The Tertiary structuration of the Western Subalpine foreland deciphered by calcite-filled faults and veins

Antonin Bilau [a,b,*], Dorian Bienveignant [b], Yann Rolland [a,b,*], Stéphane Schwartz [b], Nicolas Godeau [c], Abel Guihou [c], Pierre Deschamps [c], Xavier Mangenot [d], Benjamin Brigaud [e], Louise Boschetti [a], Thierry Dumont [b]

[a] EDYTEM, Université Savoie Mont Blanc, CNRS, UMR 5204, Le Bourget du Lac, France
[b] ISTerre, Université Grenoble Alpes, Univ. Savoie Mont Blanc, CNRS, IRD, IFSTTAR, 38000 Grenoble, France
[c] Aix-Marseille Université, CNRS, IRD, INRAE, CEREGE, Aix en Provence, France
[d] Caltech, Geological and Planetary Sciences, Pasadena, CA, USA
[e] GEOPS, CNRS, Université Paris-Saclay, 91405 Orsay, France.

ARTICLE INFO

ABSTRACT

The age of brittle deformation in the superficial part of orogens is generally constrained by relative, cross-cutting structural relationships. However, it becomes possible to decipher the timing of fault activity by a combination of methods based on U-Pb dating and stable isotope composition of calcite-filled fault and veins. This methodology is applied to constrain the timing of deformation of the frontal part of an orogenic system, through the example of the Tertiary development of subalpine massifs fold and thrust belt (composed by Bauges, Chartreuse, Vercors massifs). The architecture of the massifs is well constrained, but the chronology and the nature of involved fluids is unknown. Clumped isotope Δ_{47} analysis shows a significant variation of fluid temperature from 54 °C to the west up to 149 °C for the internal Vercors thrust to the east. These temperature estimates highlight a deep underthrusting with a significant exhumation of the eastern Vercors (4–6 km), while a shallow underthrusting at a depth of around 2 km is estimated for the central Vercors. Carbon and oxygen stable isotope analyses, reveal three fluid signatures corresponding to heated fluids from meteoric or basin-derived origin, which interacted at various extents with the host-rock. These data are in agreement with a low altitude frontal belt, and with a progressive reequilibration of downwards infiltrating fluids with the composition of the host-rocks. The successfully dated calcites are those exhibiting the highest fluid-rock ratios, which allowed U enrichment in a mainly uranium-poor rock environment. In-situ U-Pb calcite dating was performed on fault mirrors of main thrusts and on fractured pebbles of the underthrusted molasses of eight major thrusts. Preserved Oligocene ages of extensional veins related to pre-Alpine rifting demonstrate that U-Pb calcite is a robust method to characterize multiple superimposed events of a whole mountain building history. Furthermore, the presence of multiple deformation events in the same location point out the importance of inherited structures on the strain localization processes. Thrust related U-Pb on calcite ages on an E-W section between the Vercors and Chartreuse massifs record a major Miocene shortening phase, and the timing of strain propagation towards the foreland. The oldest thrust dated at 15 Ma, corresponds to the activation of the most internal preserved thrust mobilizing 149 °C fluids. In the central subalpine massifs, ages range from 14 Ma (Chartreuse) to 12 Ma (Vercors) mobilizing 54 °C fluids. On the western part, the initiation of the most external thrust has been dated between 10 Ma and 7 Ma. These geochronological constraints are consistent with an 'in-sequence' westward propagation of the deformation between 15 Ma and 7 Ma and contemporaneous with the exhumation of the Belledonne External Crystalline Massif and the development of flexural basin sedimentation. Paleostress calculations indicate a three-stage evolution of the subalpine nappe stack. Reverse and strike-slip deformations are interpreted as a diffuse tectonic reactivation in an 'hors-sequence' mode from 10 Ma to present in a broadly similar stress field.

---

* Corresponding authors at: EDYTEM, Université Savoie Mont Blanc, CNRS, UMR 5204, Le Bourget du Lac, France.
E-mail addresses: antonin.bilau@univ-smb.fr (A. Bilau), yann.rolland@univ-smb.fr (Y. Rolland).

1. Introduction

Absolute dating of brittle deformation has become possible thanks to recent developments of the U-Pb dating method on calcite (e.g., Roberts et al., 2020). This method has been applied to the reconstruction of superficial mountain belts tectonic history (e.g., Smeraglia et al., 2019; Carminati et al., 2020; Cruset et al., 2020; Curzi et al., 2021; Looser et al., 2021; Parizot et al., 2022). However, its applicability may still suffer from a lack of understanding of calcite recrystallization processes in the case of multiple stages of deformation and complex fluid history (Roberts et al., 2021). Several problems have hindered the development of this method, especially detection limits of U and Pb in calcite, which remain a major obstacle (Lanzirotti and Hanson, 1995; Chew et al., 2014). For this reason, this method was initially limited in the 1990's to calcites with high uranium contents (1–9 ppm), (e.g., Rasbury et al., 1997, 1998, 2000). A major issue has been to disentangle crystallization histories within a heterogeneous mineral at the micron scale, as the method was formerly undertaken by acid digestion and isotopic dilution (e.g., Smith and Farquhar, 1989). With the development of in-situ Laser-Ablation ICP-MS techniques (Li et al., 2014), allowing micron scale elemental mapping (Drost et al., 2018), it became possible to overcome this problem. Nowadays, the low detection limit of U and Pb (~0.1 ppm) combined to a high spatial resolution (50-150 μm spot diameter) make LA-ICP-MS dating on calcite a widely and useful method from various contexts (e.g., Roberts et al., 2021), in particular for the development and chronology of the fault network (Roberts and Walker, 2016; Ring and Gerdes, 2016; Beaudoin et al., 2018; Hansman et al., 2018; Pagel et al., 2018; Parrish et al., 2018; Hoareau et al., 2021; Parizot et al., 2021; Roberts et al., 2021; Smeraglia et al., 2021; Roberts and Holdsworth, 2022). Direct calcite dating applied to main faults along transects allows to analyse the along-belt variations of deformation ages, like the propagation of fold and thrust belts (Looser et al., 2021) and the polyphased evolution of major faults (Bilau et al., 2021; Parizot et al., 2022). The use of methods performed on calcite can brings up information on the physical and chemical parameters associated to the fluid circulation during the deformation responsible for the calcite crystallization (Goodfellow et al., 2017; Bilau et al., 2021; Hoareau et al., 2021; Looser et al., 2021) but can also be used for structural and micro-tectonic analysis to characterize the paleo-stresses recorded during the development of brittle deformation. Still, only few studies combine all these techniques. Further, it remains challenging to link these deformations and those rooted within the underlying crystalline basement which can be highlighted by thermochronological data (e.g., Girault et al., 2022).

In this paper, we focus on the Western part of the Alps, where a good geological knowledge exists for the development of the Subalpine fold and thrust belt, by paleontological indirect dating of foreland sediments (^{86}Sr/^{87}Sr on shells by Kalifi et al., 2021). Therefore, this is a suitable area for testing the U-Pb method on calcite to establish an absolute chronology and infer the duration of deformation on major thrusts. Although the sedimentary sequence is well characterized by Kalifi et al. (2021), the hypothesis of the tectonic control of sedimentation in these basins by the subsidence driven by local faults instead of a more regional subsidence, driven by European plate flexure at a larger scale, is subject to debate. Further, the possibility of testing the U-Pb calcite dating method on various objects, such as veins and fault planes related to main thrusts activity and on deformed pebbles of the underthrust conglomeratic molasse allows to test the suitability of this method. The combined geochronological (U-Pb calcite) and geochemical study (fluid proxies, $\delta^{18}O_{calcite}$ and $\delta^{13}C_{calcite}$ stable isotopes, Δ_{47} clumped isotopes) of Tertiary thrusts and molasses in the subalpine massifs, may bring absolute ages on the brittle deformation and on the conditions of calcite crystallization associated to the main tectonic events. These data are further used to reconstruct the kinematics of the Western Alps fold-and-thrust belt propagation through the (re)activation of major thrusts in the Bauges, Chartreuse and Vercors subalpine massifs, and link them to the exhumation of the External Crystalline basements.

2. Geological context

2.1. Overall structure of the Subalpine massifs

The Subalpine massifs (Bauges, Chartreuse and Vercors massifs) are part of the Alpine foreland, which correspond to the deformed Mesozoic and Tertiary sedimentary cover of the European margin in front of the exhumed External Crystalline Massifs (ECMs: Mont Blanc, Belledonne and Pelvoux). This external domain is bounded to the east by the Penninic Front, which marks the limit with metamorphic Internal Alps, representing remnants of the subducted Alpine Ocean and related extended continental margin (Fig. 1).

The foreland basin (Fig. 1) is located in front of Subalpine massifs, and consists of Tertiary sedimentary deposits over a large area. This domain shows minor deformations, such as large wave-length folds and strata tilting. By contrast, the Subalpine massifs represent a classical fold and thrust belt, which accommodated the Tertiary alpine shortening. In this context, the Tertiary sedimentary basins were locally underthrusted below the main thrusts of the Subalpine Massifs (e.g., Deville, 2021). Additionally to this thrust-controlled deformation, a mainly NE-SW dextral strike-slip fault system is present at the scale of the Chartreuse massif (Fig. 1), and appears to crosscut the main thrusts (Gidon, 1981, 1990). Despite this cross-cutting relationship, it is generally admitted that both structures were developed almost contemporaneously (Gidon, 1990). The deformation corresponds to the propagation of flat decoupling layers, mainly along the Triassic evaporites above the Paleozoic crystalline basement, resulting in a thin-skin tectonic style (e.g., Mugnier et al., 1987; Butler, 1992; Philippe et al., 1998; Bellahsen et al., 2014; Deville, 2021). To the east, the flat basal decollement roots within the basement at the western boundary of ECMs (e.g., Barfety and Gidon, 1996; Nouibat et al., 2022). In this context, the exhumation of ECMs is in part controlled by the activity of these basement thrusts combined with erosion (Bellahsen et al., 2014; Schwartz et al., 2017; Girault et al., 2022). However, the timing and geometrical relationships between exhumation of ECMs and the propagation of the frontal fold and thrust belt still suffer from a lack of direct dating constraints. The position of some of these structures seems to be highly controlled by inherited N-S extensional faults related to the Oligocene Bresse-Rhône or Jurassic Tethyan (Butler, 1992).

2.2. Timing of deformation

In the Western Alps, direct constraints of the timing of deformation are mostly gathered using *syn*-kinematic minerals within ductile shear zones in the basement (e.g., Rolland et al., 2008; Rosenberg et al., 2021). Timing of deformation within the sedimentary cover is constrained by cross-cutting relationships of the brittle structures (thrust and fault) and stratigraphic constraints on detrital material deposed within flexural basins (e.g., Kalifi et al., 2021). Underthrusting of ECMs below the Penninic Front is constrained by Ar-Ar on phengite and U-Pb on allanite in shear zones that developed within the basement between 29 and 34 Ma (Simon-Labric et al., 2009; Cenki-Tok et al., 2014; Bellanger et al., 2015). However, the timing of deformation of the Subalpine massifs, and the propagation of the frontal fold-and-thrust belt remain unconstrained by absolute dating. The relative timing of the deformation sequence is based on the deposition ages of the Neogene molasse sediments obtained by Sr isotopic ratios on bioclasts compared to the global seawater curve (Kalifi et al., 2021). These ages range between ~21.3 and 12.7 Ma (Kalifi et al., 2021) and show a westward migration of the depocenters interpreted to result from footwall tectonic subsidence in response to the activation of major thrusts (e.g., Philippe et al., 1998). However, the interpretations of the Sr isotopic ratios remain difficult to decipher between local subsidence related to thrust activity and a more regional tectonic subsidence, or even some eustatic variations. Further, due to the narrow size of intra-continental marine basins, isotopic influence of the continental source may play a significant role of the resulting sediment
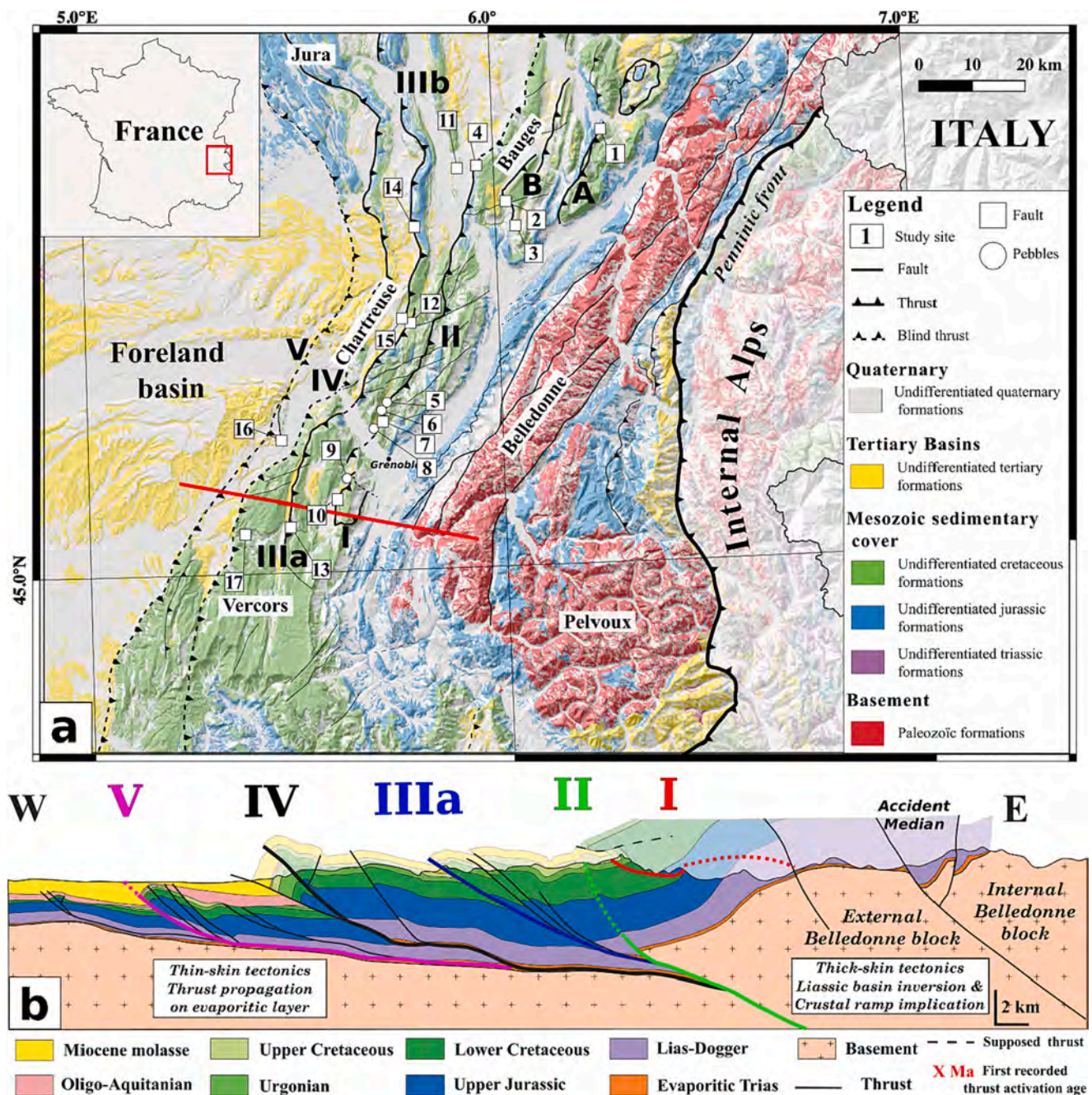
Fig. 1. (a) Geological map of Western Alps, with the location of the Subalpine fold and thrust belt massifs (Vercors, Chartreuse and Bauges) and the External crystalline massifs (Pelvoux and Belledonne). Numbers correspond to sampled locations detailed in Supplementary material 1, roman numbers and capital letters correspond to major subalpine faults and thrusts. A: Eastern Bauges fault; B: Central Bauge Thrust. I Eastern Vercors thrust; II: Eastern Chartreuse thrust; IIIa: Central Vercors thrust; IIIb: Central Chartreuse thrust; IV: West Vercors thrust; V: Western Subalpine thrust. To construct this map, the ALOS World 3D-30 m DEM (AW3D30) from the Japan Aerospace Exploration Agency (©JAXA) was used. In addition, the geo-referenced database of BRGM's 1:50,000 vectorised and harmonised geological maps (Bd Charm-50) was also used. The faults and the geological cross-section (b) are drawn from the Bd Charm-50 database and from Kalifi et al. (2021).

Sr isotopic ratios and thus resulting on significant errors on the estimated ages, which must be considered with caution. Further north, the timing of deformations in the Jura fold-and-thrust belt has been studied by in-situ U-Pb calcite dating (Looser et al., 2021; Smeraglia et al., 2021). Looser et al. (2021) constrained two successive stages in the development of the Jura between 14.3 and 4.5 Ma: (1) deformation on the basal cover-basement décollement at 14.3 ± 0.5 Ma, (2) a second phase 11.3 and 4.5 Ma, which they related to the propagation of the northern part of the Jura fold and thrust belt. Smeraglia et al. (2021) obtained similar ages within this second phase in central and southern Jura, with ages from thrusts (11.4 ± 1.1 Ma to 7.5 ± 1.1 Ma) and from

tear fault and thrust reactivations (10.5 ± 0.4 Ma to 3.9 ± 2.9 Ma).

3. Sampling strategy

Different tectonic structures related to the structuration of the subalpine foreland were targeted for this study (Fig. 2). These structures correspond to fault planes and calcite-filled fractures associated with the activation of main thrusts in the Mesozoic cover and Tertiary molasses (Fig. 2). This fracturing is recorded by centimetre scale calcite filled-veins within pebbles from the Neogene conglomeratic molasses. The post-deposition nature of the deformation is certified by an observable
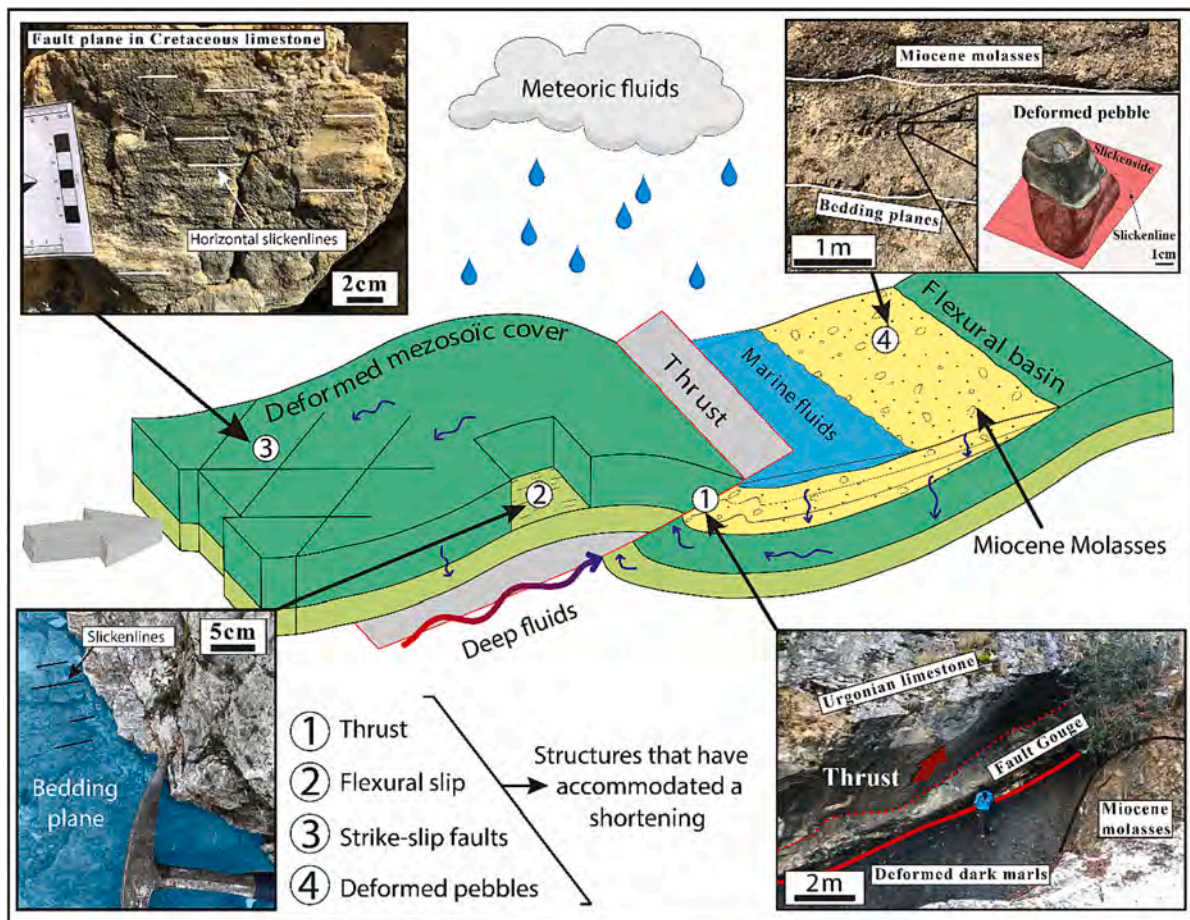
Fig. 2. Sketch illustrating the different types of studied structures and their relative position to the thrust. Four types of structures have been studied and sampled: (1) main thrusts in the Mesozoic sedimentary cover, (2) Strike-slip faults and (3) flexural slip fault in the hanging wall of the thrust, associated to the ramp anticline development, (4) fractured pebbles with calcite filling in the molasses.

offset between each side of the fracture calcite filling-vein, see section 4.2. Each sample location has been numbered in the Fig. 1. GPS data, names and other information are included in the Supplementary material 1. Field photographs of outcrops are displayed in Supplementary material 2.

### 3.1. Striated fault planes and veins

We sampled slickenfibres and calcite filled-veins kinematically linked to major thrust and strike-slip faults. Field structural analyses have been performed on 16 locations from the three Subalpine massifs (Fig. 1). In the Vercors massif central part, at Rencurel (location 13 in Fig. 1), the so-called "Urgonian" (i.e., Aptian-Barremian) limestone is thrusted towards the NW above unknown age dark marls and Miocene molasses (Fig. 3). The fault zone is marked by a meter-scale fault gouge. The hanging wall of the thrust is marked by a main striated plane oriented ~N10°E. The dark marls are highly deformed with C-S fabrics that locally encloses fragment of calcite veins (Fig. 3). These veins are related to early deformation stage of central Vercors thrust (Roberts, 1994). The fault gouge (sample B, Fig. 3a), a fragment of calcite filled-vein in C-S fabric in the dark marls (sample A) and an undeformed sample taken as reference of the Urgonian hanging wall were sampled.

In the Bauges massif (location 1, Thrust A), fault gouge was collected in a reverse fault N146°E crosscutting Urgonian limestones (Supplementary material 2). No clear tectoglyphs indicate weither normal or reverse movement occur but in spite of the low inclination (~20°NE) it has been considered as a reverse fault. At location 2 thrust B (Fig. 1) a sample was collected in Upper Valanginian carbonates on a metre-scale

top-to-the-west reverse fault plane (oriented N145°E). In the continuation of the fault from location 2, at location 3, the sample was collected in Urgonian limestones on a sinistral strike-slip fault (oriented N64°E). The sample from location 4 corresponds to a fault gouge developed in Urgonian limestones with sigmoidal structure exhibiting reverse top-to-the-west kinematics related to thrust II (oriented N132°E). At location 11, the sample was collected on a N19°E dextral strike slip fault plane also in Urgonian limestones (Supplementary material 2).

In the Chartreuse massif the sample from location 12 was collected in Valanginian carbonates along a reverse fault plane (N11°E) related to thrust IIIa. At location 14 the sample was collected (location 14 in Fig. 1) in massive Portlandian carbonates, along reverse top-to-the-west fault plane (N170°E) associated to a pop-up structure combined to ramp anticline of thrust IIIb. Further south, on the same thrust, at location 15, decametre fold in Urgonian have been observed and a decimetre reverse fault plane (N43°E) have been sampled. In the south-eastern part of the Chartreuse massif, at location 7, the sample was collected in lower Valanginian carbonates along N111°E sinistral strike-slip faults (Supplementary material 2).

In the NE of the Vercors massifs, at location 10, the sample was collected on a N85°E dextral strike-slip fault plane in limestone from the hanging-wall of the top-to-the west eastern Vercors thrust I. At the western most location 16 in Urgonian limestones, sample A on normal fault plane (N16°E) and sample B from a fault gouge (N37°E) resulting from flexural slip were selected. These structures are interpreted as related to a top-to-the-west thrust fault V and related to the ramp anticline development during the NW-SE compression. The last location (17) with Upper Valanginian limestones shows three types of structures, (1)
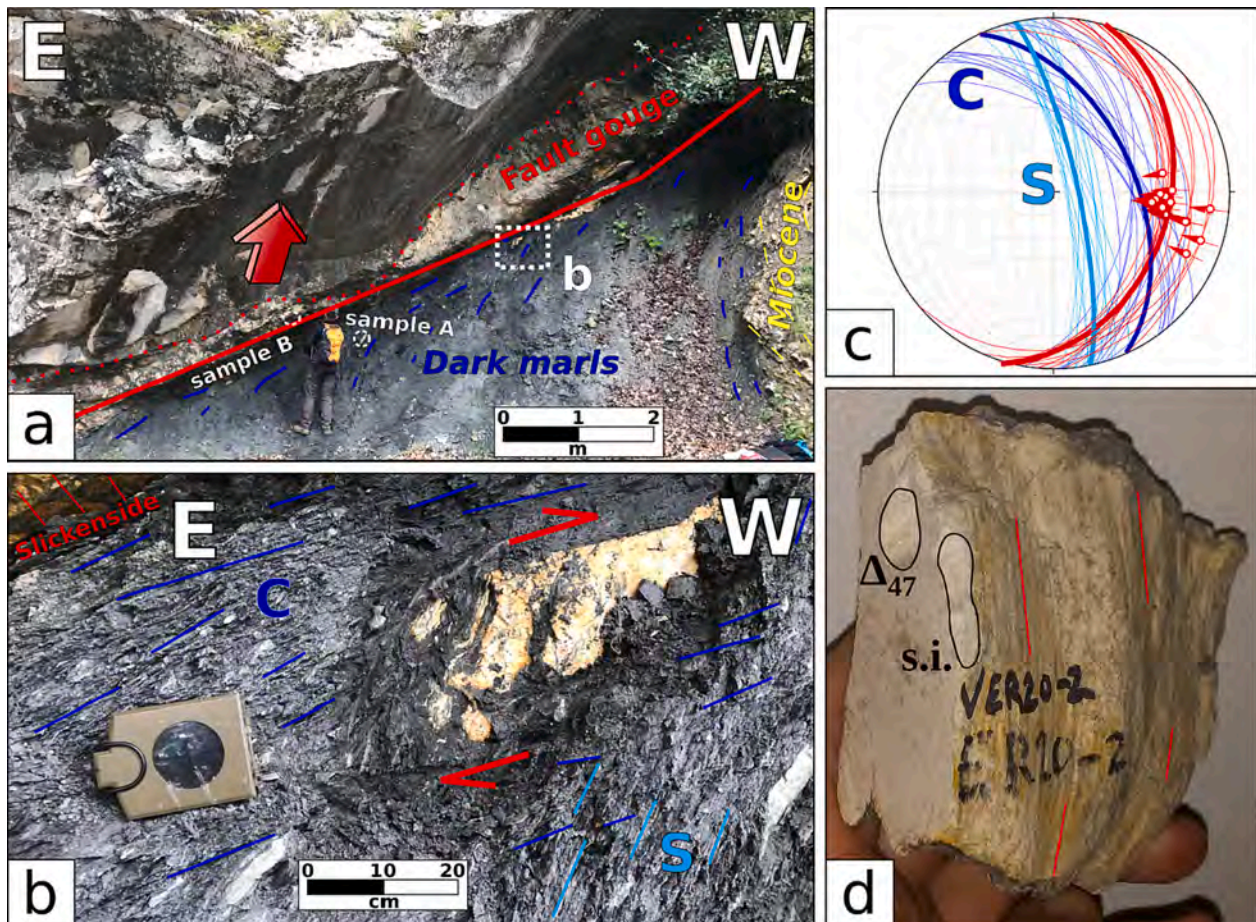
Fig. 3. (a) Field photographs of central Vercors thrust (Rencurel, location 13 in Fig. 1) with Urgonian, main fault plane in red and related cleavage in slates of the high-strain zone in blue. (b) Zoom on a calcite sigmoid close to the fault plane and C-S fabrics. (c) Stereogram of the fault planes, Urgonian bedding and dark marls cleavage, colours refer to (a). (d) Photography of calcite fault gouge sample B with sampling spots of $\Delta 47$ and stable isotopes (s.i.) with slickensides underlined in red. (For interpretation of the references to colour in this figure legend, the reader is referred to the web version of this article.)

vertical large extensional decimetre-scale calcite veins (N28°E); (2) strike-slip oblique fault planes (N104°E); (3) reverse fault plane (N169°E). Type (1) and (2) where sampled, but only (1) was dated. In this outcrop, the cross-cutting relationships is evidenced by reverse fault planes displacing the vertical veins, which are clearly older (see Supplementary material 3).

3.2. Fractured pebbles

The conglomeratic Miocene molasses are located on the footwall of several thrusts. In footwall basins bedding can be tilted due to the flexuration relative to the above thrust, see local geologic cross-section in Supplementary material 4. The polygenic pebbles of the molasse include a variety of limestones and ophiolite blocks (meta-basalt, gabbro, serpentinite) from a more internal origin. Highly deformed pebbles were observed, especially in the eastern side of the Vercors-Chartreuse massifs (Fig. 4). The tectonic structures include calcite filled-fractures with clear offsets, highly elongated pebble with a thin cleavage and dissolving cups exhibiting pressure-dissolution processes (Fig. 4c). The limited number of locations where the tectonic analysis is possible is due to (1) sandstone dominance versus conglomeratic lithology in the molasses and (2) an overall low density of fracturing within the pebbles, mainly concentrated at the proximity of faults.

Fractured pebbles were sampled at location 9 associated to Thrust I and at three locations in south-eastern Chartreuse associated to Thrust II at locations 5, 6 and 8 (Supplementary material 2).

At location 8, bedding is sub-horizontal and three distinct fractured

pebbles were dated. At location 6, close to the thrust, pebbles are less deformed than at location 9, but the molassic bedding is vertical. Location 5 also exhibits highly deformed molassic pebbles.

4. Methods

4.1. Stable isotopes analyses

In this study, $\delta^{13}C$ and $\delta^{18}O$ ratios were acquired using two methods: (1) by isotope ratio mass spectrometer (IRMS) on calcite powders sampled with a dental micro-drill with a diameter of 1 mm (host-rock and calcite cement independently) and (2) by secondary ion mass spectrometry (SIMS) on polished thin-sections, using the Ion Mass Spectrometer (IMS) 1280 (CAMECA) at the Centre de Recherches Pétrographiques et Géochimiques (CRPG) in Nancy, France. Four types of calcites have been sampled: calcite filled-fractures within pebbles (fractured pebbles from location 6, 8 and 9), fault gouge calcite filling of thrust and calcite filled-veins cross-cutting the fault gouge (from location 1, 13, 14, 15) and mineralized fault plane (location 3, 7, 10, 12). For the IRMS, 11 carbonate powders were analysed using a dual-inlet Isoprime 100 spectrometer (Elementar) coupled to a multiCarb system to determine O and C isotope compositions of calcite at the Laboratoire des Sciences du Climat et de l'Environnement (Université Paris-Saclay). Data were standardized to Pee Dee Belemnite (PDB) based on repeated measurements of international reference materials NBS19 and NBS18, with respective values of $-2.20‰$ and $-23.01‰$ in PDB for $\delta^{18}O$ and $1.95‰$ and $-5.01‰$ in PDB for $\delta^{13}C$. The reported
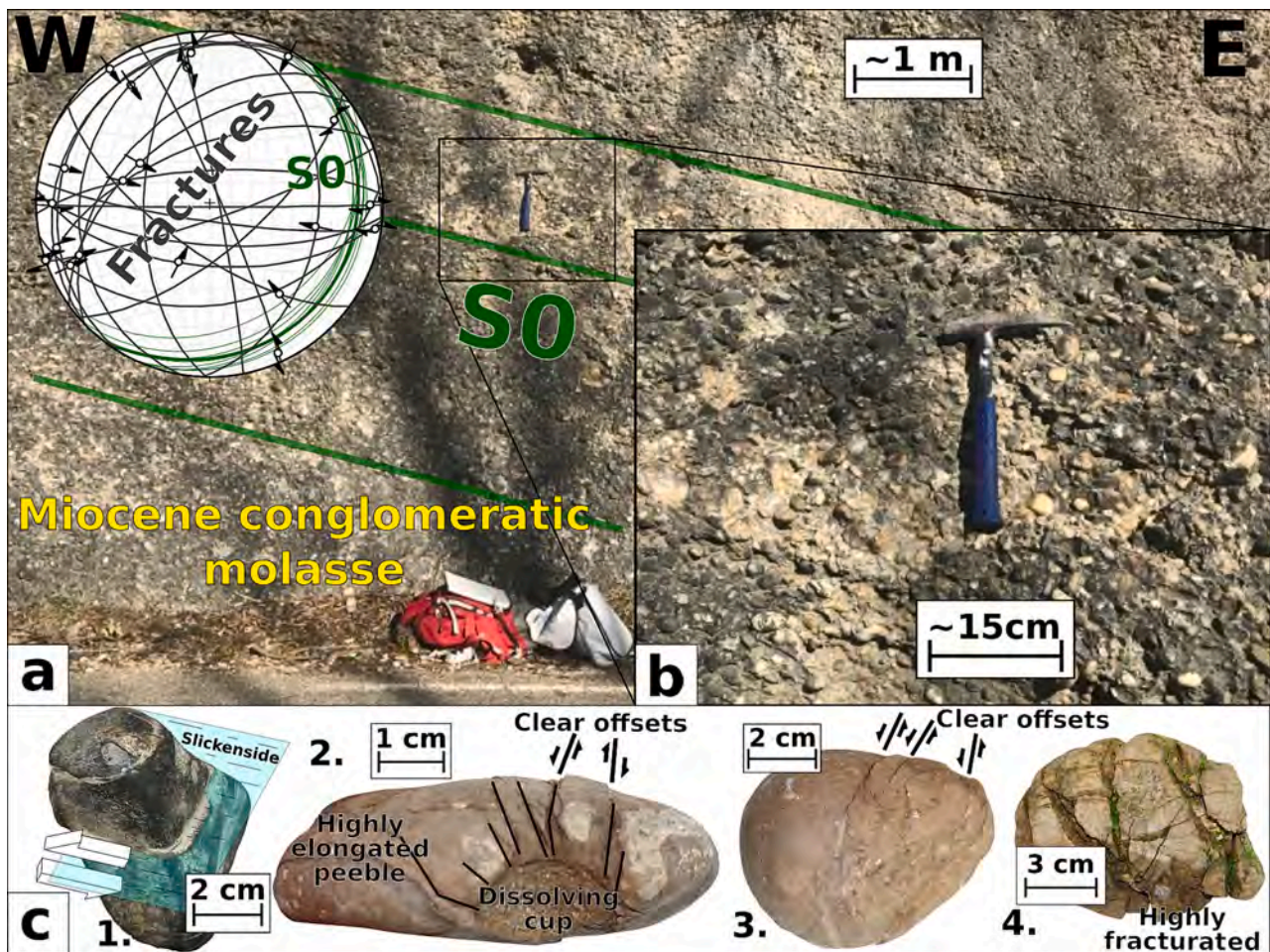
Fig. 4. (a) East Vercors location 9 Miocene conglomeratic molasse with (b) zoom and corresponding stereoplot of fractures (in black) and bedding (in green, 'S0'). (c) Examples of strained pebbles figures exhibiting brittle-ductile deformation: 1, Visible fracture with mm displacement highlighted by slickensides; 2, Dissolution cups with linked radial fracturing and offset; 3, Small calcite filled-veins with observable offsets; 4, Widespread fracturation and fibrous crystallization without any visible offset. (For interpretation of the references to colour in this figure legend, the reader is referred to the web version of this article.)

uncertainties are based on the external reproducibility of an in-laboratory carbonate standard (MARGO) with 1SD of 0.05‰ for $\delta^{18}O$ and 0.03‰ for $\delta^{13}C$. For the SIMS analysis, 5 thin sections were analysis for a total of 17 $\delta^{13}C$ and $\delta^{18}O$ ratios on calcite and dolomite according to the methodology described by Andrieu et al. (2018) and Peyrotty et al. (2020). Thin sections were cut in order to match the 30 × 23 mm sample-holder and were coated with gold before the analysis. The sample is exposed to a primary beam of Cs^+ ions under a vacuum down to few mbar. The primary ion beam diameter varied from 20 μm for oxygen isotope measurements to 10 μm for $\delta^{13}C$ carbon isotope measurements, and the depth of the resulting crater was <1 μm. The 2σ error range varies from 0.15‰ to 0.35‰ for oxygen isotopes, and from 0.2‰ to 1.3‰ for carbon isotopes. The calibration standard used was a calcite crystal (CCigA) with a $\delta^{18}O$ value of 18.94‰ SMOW (Standard Mean Ocean Water) and a value of 1.04‰ PDB for $\delta^{13}C$ and a dolomite crystal with a $\delta^{18}O$ value of 20.04‰ SMOW (Standard Mean Ocean Water) and a value of 3.56‰ PDB for $\delta^{13}C$. For a complete description of the materials and protocol, refer to Rollion-Bard et al. (2007). All results are presented in per mil (‰) deviation from the PDB standard (‰ PDB).

4.2. Clumped isotope analyses

Clumped isotope Δ_{47} analyses were performed to infer temperature and $\delta^{18}O$ of the fluid during calcite crystallization (Ghosh et al., 2006; Eiler, 2007; Huntington et al., 2009; Pagel et al., 2018; Mangenot et al., 2019; Brigaud et al., 2020). Thirty mg of calcite was sampled using a

dental micro-drill with a diameter of 1 mm. Clumped isotope Δ_{47} measurements were performed at the California Institute of Technology (Caltech, USA) with an automated acid digestion and gas purification device coupled to a dual inlet Thermo MAT253, as described in Passey et al. (2010). Samples were weighed into silver capsules (~ 8 mg) and reacted in a common phosphoric acid bath (~ 103%) for 20 min at 90 °C under static vacuum. The resulting CO_2 was passed through an ethanol/dry ice U-trap (~ −80 °C) before being collected on a liquid nitrogen temperature (−196 °C) U-trap. Following the 20 min reaction period, the collected CO_2 was thawed, entrained in helium, and carried through a Porapak Q 120/80 mesh gas column held at −20 °C using He as the carrier gas. The purified CO2 was analysed using a Thermo Scientific MAT 253 Mass Spectrometer set to collect masses 44–49. Mass 48 was only monitored to detect any hydrocarbon contaminant. $\delta^{18}O$ and $\delta^{13}C$ data was also acquired as part of each Δ_{47} analysis and calculated using the parameters reported relative to the PDB reference frame based on the calibrated composition of the laboratory working gas and the correction scheme and constants from Brand et al. (2010). In order to account for the temperature dependence of oxygen isotope fractionation between CO_2 gas and carbonate resulting from the reaction with phosphoric acid at 90 °C, a fractionation factor of 1.00811 was used for calcite following Swart et al. (1991). The raw Δ_{47} data was corrected for instrument non-linearity and scale compression (Dennis et al., 2011) using several heated (at 1000°) and equilibrated gases (at 25 °C) of various bulk isotopic compositions that were run during each session. These gases were used to convert measurements into the inter-

laboratory absolute reference frame (Dennis et al., 2011). To guarantee accuracy of the Δ_{47} data, we routinely analysed two carbonate reference materials (Carrara marble and TV04). One of these two carbonate standards was analysed once for every five analyses of the unknown samples in order to check for procedural analytical stability and accuracy, and to determine the long-term external reproducibility of our measurements. The Δ_{47} values obtained for these carbonates over the course of this study (April to July 2021) are: $\Delta_{47\text{-CDES25}} = 0.409 \pm 0.016$‰ ($1\sigma$, $n = 10$) for Carrara; $\Delta_{47\text{-CDES25}} = 0.666 \pm 0.011$‰ ($1\sigma$, $n = 8$) for TV04, i.e., within accepted Δ_{47} values for TV04 ($\Delta_{47\text{-CDES25}} = 0.655$‰) and Carrara ($\Delta_{47\text{-CDES25}} = 0.405$‰). Finally, the corrected Δ_{47} values were converted into temperatures using the composite $\Delta_{47\text{-T}}$ calibration of Bonifacie et al. (2017), which has been shown to be appropriate for calcite and dolomite between 0 and 300 °C, and which has been shown to be consistent with measurements made at Caltech. The oxygen isotopic compositions of the fluid ($\delta^{18}O_{\text{Fluid}}$) from which the carbonates precipitated were calculated for each estimated TΔ_{47} using the bulk $\delta^{18}O_{\text{calcite}}$ values and the calcite-water fractionation equation from Kim and O'Neil (1997).

4.3. Paleotensors

Three types of calcite-filled fractures have been characterized in the field: (1) striated fault plane, (2) fault gouge cement with sigmoidal shear structures, (3) calcite filled-veins of fractured pebbles from Neogene conglomeratic molasses. Standard azimuth and plunge measurements have been performed on fault planes of structures (1) and (2). For the structures (3) measurements were done on endured fractured pebble with observable offset along the fractures. In rare cases, slickensides are observed so, standard measurements were made. Otherwise, slickenside direction is regarded as equivalent as the maximal displacement line between the two sides of the pebble and perpendicular to the pebble surface. The sense of the movement is indicated by the relative displacement between the two sides. Structural data are sorted in population based on field identified generation and conjugated families (Pascal, 2021). Inversions have been done with TectonicsFP (Ortner et al., 2002) using NDA method (Numerical method for Dynamic Analysis described in Spang, 1972. The NDA results are plotted as right dihedral diagrams (Angelier and Mechler, 1977) with a compressive (black) and extensive (white) quadrant containing respectively $\sigma 3$ and $\sigma 1$ principal stress axis. The P-B-T kinematic axis calculation (Turner, 1953; Marrett and Allmendinger, 1990) allows to obtain the principal stress axis orientation (Ortner et al., 2002). The P-B-T axis of each fault plane are plotted in a lower hemisphere with an equal-area stereographic projection. For each location, inversion have been done with a 30° frictional internal angle "theta" (mean value for undifferentiated type of rocks) and then with the best-fit calculated angle. TectonicsFP also calculate fluctuation histograms of the differential angles between the direction of the measured striae and the direction of the calculated shear stress related to the data inversion. The larger the part of the dataset close to 0 is, with a rapid decrease, the better it is, but no secondary maximum should be recorded. In the following results, based on Mohr circle visualization, the result with the most significant mechanical consistency is selected. This verification step is required in order to eliminate physically aberrant cases possibly deducted from the calculated best-fit of frictional internal angle.

4.4. U-Pb calcite dating

In-situ U-Pb calcite analyses were carried out at the CEREGE (Centre Européen de Recherche et d'Enseignement des Géosciences de l'Environnement), Aix-en-Provence, France. On each thin-section, petrography using optical microscope, cathodoluminescence and SEM were done in order to identify multiple calcite generations. In some samples, variations of calcite texture have been recorded (coexistence of fibrous and blocky calcite filled-veins, Fig. 10 and Supplementary material 5).

Analyses were carried out using the parameters given in Supplementary material 6 (adapted from Ganade et al., 2022). For data processing, raw intensities and baseline correction were made with Iolite 3 (Paton et al., 2011). Instrumental drift based on NIST614 analyses (Woodhead and Hergt, 2001), Pb isotopes composition and $^{206}Pb/^{238}U$ are calculated using an in-house Python code. Spots with mean ^{207}Pb intensities below 3 times the baseline intensity were excluded. Tera-Wasserburg plots were made using IsoplotR (model-1), intercept ages and initial Pb composition (Vermeesch, 2018). Ages are quoted at 2σ absolute with propagation of WC1 2.51% age error by quadratic addition (Roberts et al., 2017). Excess variance of reference material is propagated into sample data. Systematic uncertainties include age uncertainty of reference material.

5. Results

5.1. Stable Isotopes

46 samples have been analysed (32 in dissolution and 14 in SIMS). Corresponding $\delta^{18}O_{\text{calcite}}$ and $\delta^{13}C_{\text{calcite}}$ results are displayed in Supplementary material 7 and have been plotted in Fig. 5.

5.1.1. Host-rock compositions

A total of eleven analyses has been made on pebbles and carbonate host-rocks. On Fig. 5, these data appear to plot in a restricted field, close to previously published data from the Jura (Smeraglia et al., 2020; Looser et al., 2021). This field ranges from −6 and − 3‰ $\delta^{18}O$ ratios and from −1.7 to 2‰ $\delta^{13}C$ ratios, which is thus considered as the 'host-rock buffered domain'.

5.1.2. Host-rock buffered veins

A minority of calcite vein samples from our dataset (8/35 values) show a composition close to the host-rock isotopic signature (Fig. 5). These values are obtained in veins from strained pebbles. This 'host-rock buffered' domain comprises different types of calcite veins, large calcite filled-veins (few cm in width) with ~100 μm blocky calcite, medium-size calcite veins (mm in width) with fibrous calcite and small size calcite filled-veins (100–1000 μm width) with either fibres or elongated to blocky calcite (Supplementary material 5).

5.1.3. Unbuffered calcites

A majority of calcite vein samples from our dataset (23/35 values), in either fault zones or strained pebbles, show a composition distinct to the host-rock isotopic signature (Fig. 5). These veins show $\delta^{18}O$ ratios that are significantly lower (−12.5 to −8.6 ‰) and $\delta^{13}C$ ratios slightly lower (up to −2.5‰) than their host-rocks. This trend of values is consistent with previously obtained vein values from the Jura Massif (Smeraglia et al., 2020; Looser et al., 2021). In detail, some calcites, like location 8 in the Chartreuse massif, plot at the boundary of the host-rock buffered domain showing a slight $\delta^{18}O$ depletion of −6.9‰ while bearing a $\delta^{13}C$ signature similar to the host-rock (−1.9‰). Similarly, at location 9, a calcite vein from a fractured pebble presents a $\delta^{18}O$ ratio of −6.2‰ and $\delta^{13}C$ ratio of 2.5‰, slightly distinct from its host-rock. Similarly, in the Bauges massif, samples from location 1 and 3 plot at the boundary of the 'unbuffered domain' and exhibit depleted $\delta^{18}O$ values (−7.7‰ and − 7.1‰, respectively) and similar $\delta^{13}C$ values (1.1‰ and 0.2‰) compared to their host-rocks.

5.2. Δ_{47} Analysis

Two Δ_{47} analyses were made in the Vercors massif: east Vercors (location 9) and central Vercors (location 13) (Table 1). The associated error of 0.014 is the 1σ analytical error obtained on the standard replicates ($n = 18$). At location 9, a $\Delta_{47\text{CDES90}}$ value of 0.363 ± 0.014 has been obtained for a large fibrous calcite filled-vein (Supplementary material 5) from a pebble sample corresponding to a temperature of 149
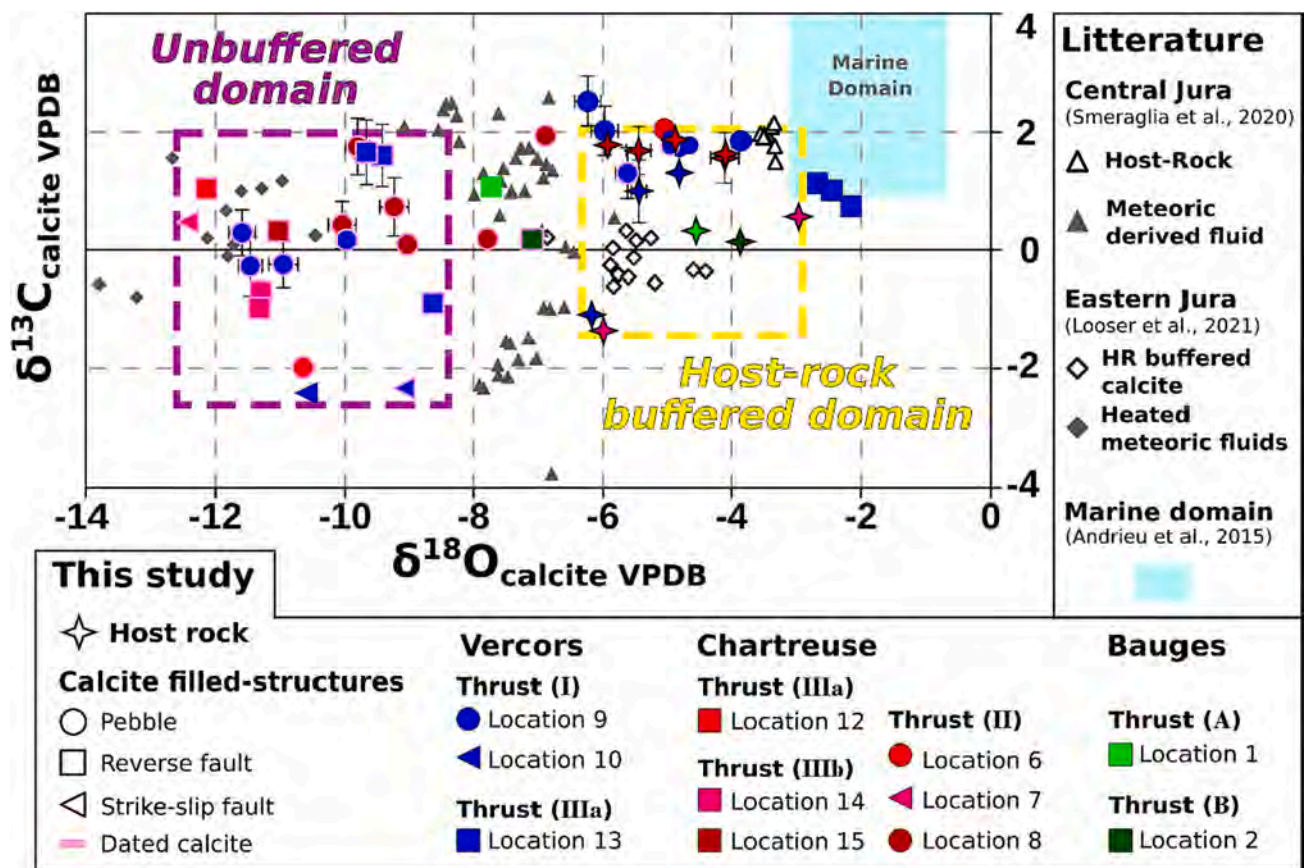
Fig. 5. $\delta^{13}C_{calcite\ (VPDB)}$ versus $\delta^{18}O_{calcite\ (VPDB)}$ plot. Dotted frames are identified domains based on our data. Error bars (at 2σ) for conventional isotopic analysis are smaller than symbols and those for SIMS analysis appear to be much larger. Letters and roman numbers correspond to main thrusts (Fig. 1).

Table 1
Clumped isotopes results. $\delta^{18}O_{fluid}$ are calculated with Kim and O'Neil (1997) equation.

Location	$\delta^{18}O_{calcite\ (VPDB)}$	$\delta^{13}C_{calcite\ (VPDB)}$	Δ^{47}_{CDES90}	1σ	Δ^{47} min	Δ^{47} max	T°C	1σ	T°C min	T°C max	$\delta^{18}O_{fluid\ (SMOW)}$
Location 9	−4.4	2.0	0.363	0.014	0.349	0.376	149	12	137	161	15.9
Location 13	−2.7	1.0	0.521	0.014	0.508	0.535	54	6	48	60	5.0

± 12 °C. At central Vercors (location 13), a $\Delta_{47CDES90}$ value of 0.521 ± 0.014 has been obtained for a fault gouge cement sample corresponding to a crystallization temperature of 54 ± 6 °C (Table 1). Combining calcite $\delta^{18}O$ signature and crystallization temperature allows the calculation of $\delta^{18}O_{fluid}$ signature using Kim and O'Neil (1997) fractionation equation. By using this equation, we obtained a value of 15.9‰ $\delta^{18}O_{fluid\ (SMOW)}$ ratio for east Vercors, while a value of 5.0‰ $\delta^{18}O_{fluid\ (SMOW)}$ is obtained for the central Vercors sample (Table 1). The nature of circulating fluids using these data will be discussed in section 6.3.

5.3. Paleo-stress tensors

Fault data inversion results are shown on (Fig. 6) and Supplementary material 8. Over the whole study area, reverse and strike-slip faults have been measured in the vicinity of the main thrusts of the subalpine massifs (Bauges, Chartreuse, and Vercors). In the field, the relative chronology established between these two fault types shows the anteriority of the reverse compared to the strike-slip tectonics (see Supplementary material 3 relating to the description of location 17 where a relative chronology is established). In total, the fault data inversions yielded 18 reduced stress tensors and their respective histograms (Fig. 6).

5.3.1. Fractured pebbles in the molasse sediments

In the conglomeratic molasse formations, three reduced tensors were obtained at locations 6, 8, and 9. The orientations of the measured faults are inhomogeneous (in orientation and movement). This can be seen in the Angelier plots, in the weak groupings of the P-B-T axes, and in the histograms obtained (several maxima are observed in the histograms, and errors >45° are visible). In these molasses, inverse regimes with E-W to NW-SE compressional axes (P-axes varying approximately between N87°E and N120°E) were found. The dip of the S0 planes measured at these locations varies between 19 and 82° and no data tilting was performed.

5.3.2. Striated fault planes in thrusts crosscutting the Mesozoic sediment cover

Seven tensors with compressive regimes were obtained (vertical σ3 axis; see locations 2, 12, 13, 14, 15, 16 and 17). Fault plane dip azimuth are from N330°E to N100°E (mainly N90°E) and dip of ~30 to 75° (Fig. 6 and Supplementary material 8). E-W compressional axes were obtained for almost all results (orientation of the P-axes oscillating globally between N89°E and N105°E). Only locations 14 and 15 show an NW-SE compressional axis (P-axis orientation ~N130°E). The P-B-T axes have low dispersion and the histograms obtained also show errors <30°. As for the strike-slip tensors, low inhomogeneity of the data sets is
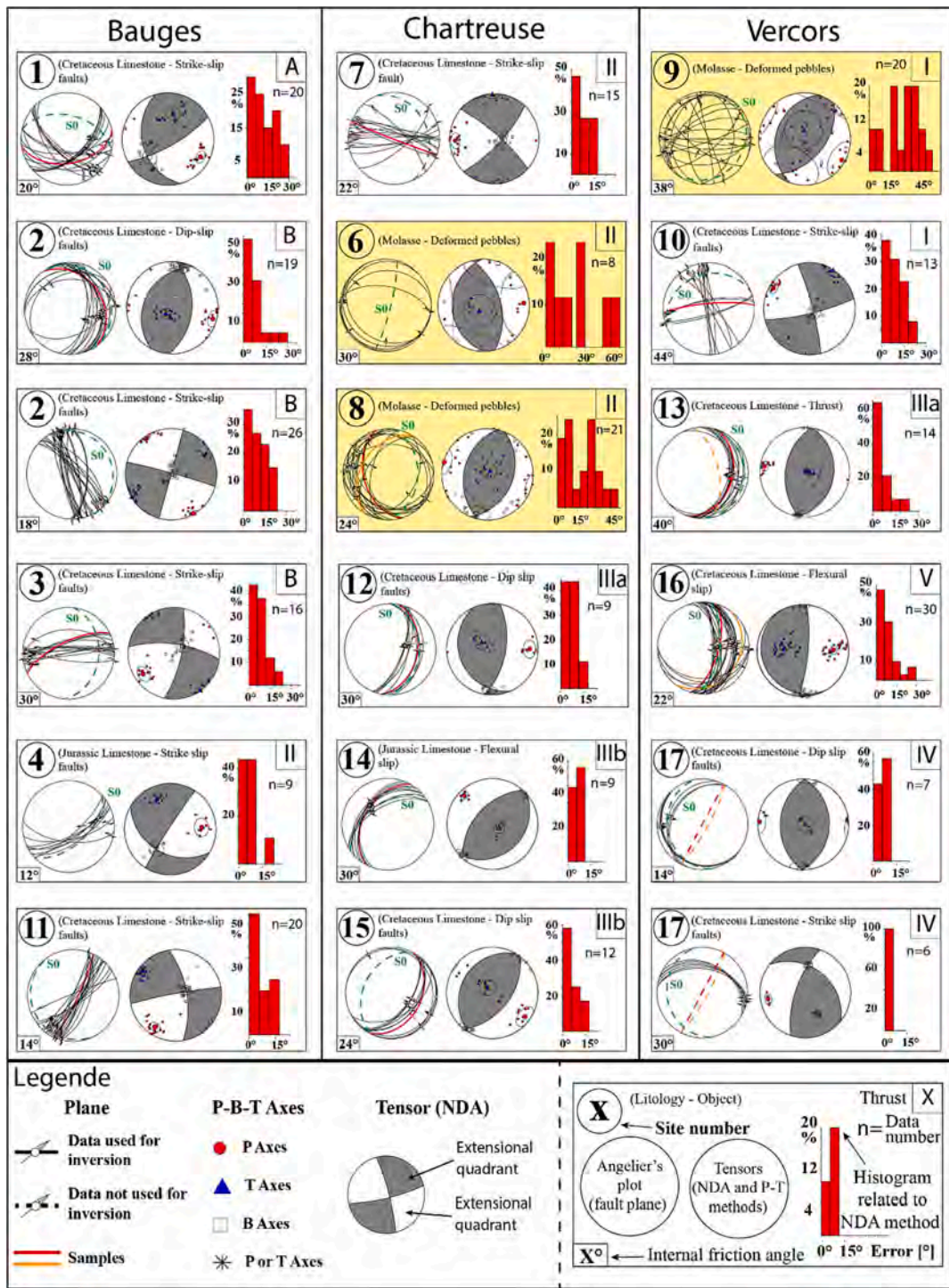
Fig. 6. Calculated tensors based on fault orientations, displacement and striae data. Black and white quadrants correspond to compression and extension quadrant, respectively. The P, B and T axes are represented by red circles, white squares and blue triangles respectively. Numbers correspond to the location of measurements (Fig. 7). For each study location, the orientation of the fault planes and their striations as well as the stratification planes (S0) are given in the Angelier plots. In addition, the orientation and name of the samples taken for U-Pb dating are also shown in the latter (coloured in red and orange for samples A and B). The dotted planes are not included in the data inversions (such as the S0 planes and the samples from location 17 which correspond to extensional vein orientations). For each location, the results of the inversions are displayed as right dihedral diagrams (NDA method) and P-B-T axes (P-T method). In addition, histograms related to the NDA method are given. (For interpretation of the references to colour in this figure legend, the reader is referred to the web version of this article.)

visible in the histograms of locations 14 and 17. It is worth noting that at locations 3, 4, 12, 13, 14, 15, and 17 described above, a monotonic attitude of the fault planes is observed in the Angelier plots. On the contrary, the results of the inversions carried out on locations 1, 2, 7, 10, 16, and 17 are constrained by the presence of conjugate faults or by

distinct fault orientations.

5.3.3. Strike-slip faults

The faults measured in Jurassic and Cretaceous limestones in the study area yielded eight tensors with strike-slip regimes (horizontal σ1

and σ3 axes; see locations 1, 2′, 3, 4, 7, 10, 11 and 17). In the case of strike-slip faults, E-W to NW-SE compressional axes (P-axis oriented N88°E to N148°E) are observed at locations 1, 2′, 7, and 10 computed with both dextral and sinistral fault planes (Fig. 6, Supplementary material 8). The tensors at locations 3, 4, 11 and 17′ are consistent with a NE-SW compressional axis (~N36°E to ~N80°E) computed with both dextral and sinistral fault planes. However, it should be noted that small inhomogeneities of the data are observed in the histograms of locations 1, 4, and 11. At location 17, vertical extensional veins were sampled and the structural measurements of these veins are not taken into account in the data inversion, so no tensor can be related to the dated sample. At the latter location, only a relative chronology shows that the extensional veins predate the reverse faults, which also predate the identified strike-slip tectonics. Furthermore, the two inversions at location 17 are constrained by a small number of data (<8 data) whereas at the other study locations, between 8 and 30 data per location could be used for the inversions.

5.4. U-Pb dating

In this study, we present 27 in-situ U-Pb ages on calcite from 17 different locations spread in Bauges, Chartreuse and Vercors massifs, ordered from east to west (Fig. 7, data are available in Supplementary material 9). In Miocene pebbles, a total of 10 ages were obtained from 4 locations while for fault plane a total of 17 ages have been obtained from 13 locations (Fig. 7).

For each of the three sample types (mineralized striated fault plane, fault gouge cement and filling-veins) success rate was about 60% (27 ages out of ~45 screened thin-section) with the highest rate for in filling veins of fractured pebbles (65% with 9 samples over 14 gave at least 1 age).

The following ages are presented with a 2σ error bar (including error propagation of WC-1 uncertainties). All the obtained ages presented below have satisfactory MSWD values mostly around 1, with several ages showing a slightly higher value (up to 4.5).
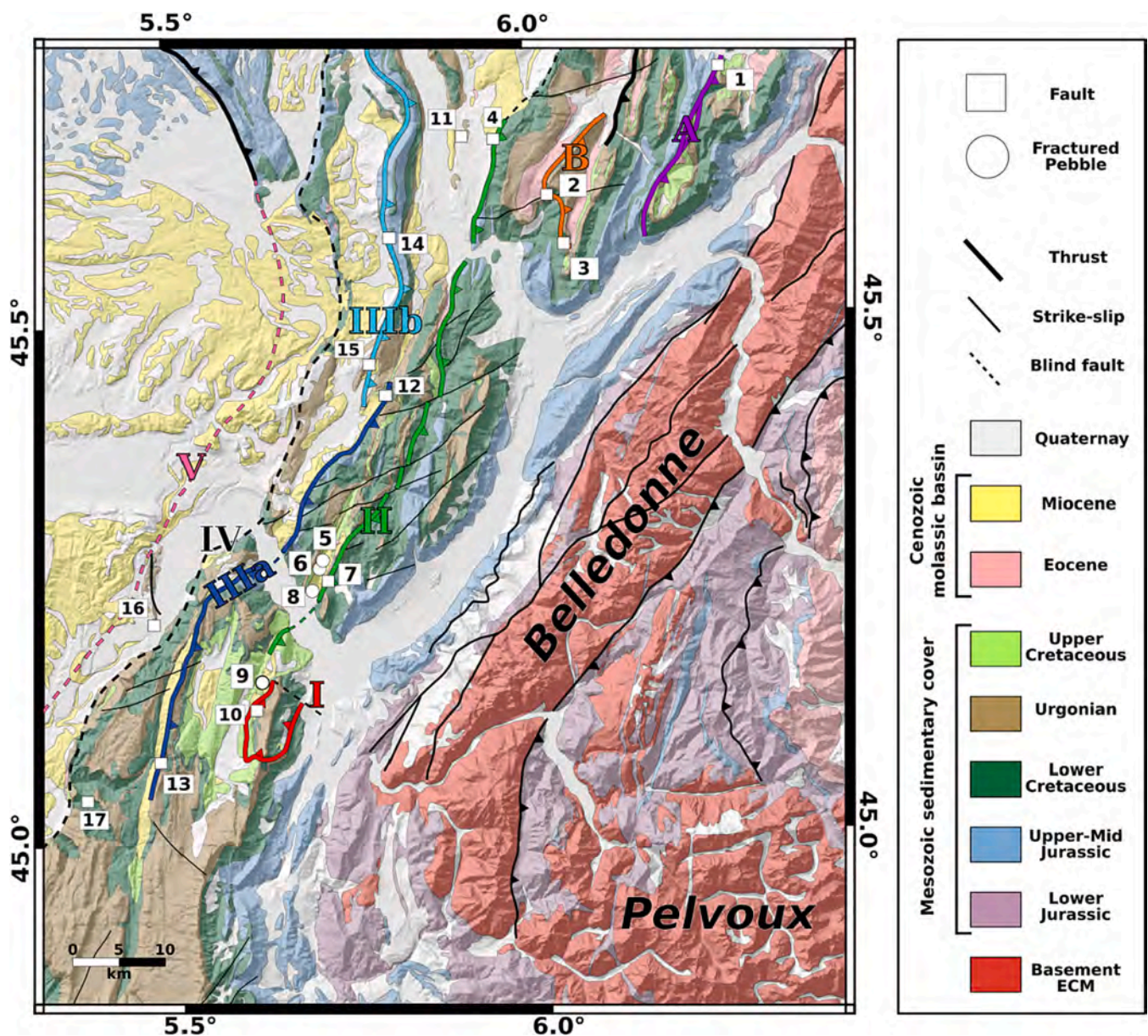

Fig. 7. Simplified map with main thrusts and minor faults and sampled location, see Fig. 1 caption. Roman numbers refer to the thrust relative chronology.

5.4.1. Dating the extension

In south-western Vercors massif, at location 17, large (decimetre scale) N-S trending vertical veins related to an *E*-W extensional stress field (Supplementary material 3), gave a maximum age of 32.3 ± 0.8 (MSWD = 1.3), significantly older than for the rest of the fault planes. However, dispersion of the U-Pb results is interpreted as resulting from variable U and Pb mobilization - open-system behaviour - suggesting calcite recrystallization (Roberts et al., 2021). It is noted that a second group of U-Pb results intercept the concordia at 23.8 Ma. Consequently, we interpret these two ages as related to two stages of crystallization during the Oligocene extensional phase at 32 and 24 Ma.

5.4.2. Dating the compression

5.4.2.1. Bauges massif.
East of the Bauges massif, at location 1 (Thrust A; Fig. 8), a calcite-filled fracture within the largest reverse fault has been dated at 5.7 ± 1.6 Ma (MSWD = 1.5). The next thrust to the west (B in Fig. 8) has been dated in locations 2 and 3 (Fig. 8). At location 2, a reverse fault plane returned an age of 6.5 ± 1.2 Ma (MSWD = 3.5). The relatively large error obtained on the age and on individual spots is due to their low Pb contents. Although the MSWD is relatively high, the robustness of this isochrone is provided by an important spread in $^{238}U/^{206}Pb$ ratio over 0 to 450. At location 3, the collected sample corresponds to strike-slip fault plane along the same Thrust B structure. It has been dated by at 12.2 ± 0.8 Ma (MSWD = 4.5). This relatively high MSWD is due to a significant variability of $^{207}Pb/^{206}Pb$ ratios for a given range of $^{238}U/^{206}Pb$ ratios, but can be also explained by the high number of spots ($n = 89$), thus the reliability of this age remains high. The robustness of this isochrone is provided by the spread in $^{238}U/^{206}Pb$ ratio over 0 to 350. To the north of Chambery, in the central part of the Bauges massif (location 4, Thrust II), an age of 7.5 ± 1.9 Ma (MSWD = 5.8) has been obtained on a gouge calcite cement within a reverse fault zone. A lot of spots were discarded after ^{207}Pb cut-off leaving only 10 spots and a relatively important error bar. Although, the remaining spots shown a sufficient spread in $^{238}U/^{206}Pb$ ratios from 100 to 600, this age is thus taken as indicative (Fig. 8). At the eastern limit of the Bauges massif, at location 11, an age of 16.5 ± 0.5 Ma (MSWD = 1.7) has been obtained from a N34° vertical (dextral) strike-slip fault plane. This fault plane does not seem to be related to any major thrust (Fig. 7).

5.4.2.2. Chartreuse massif.
To the south-east of the Chartreuse massif, three locations associated to Thrust II have been dated (Fig. 7, Fig. 9). A consistent age has been measured at locations 5 and 6, of 12.7 ± 0.8 Ma (MSWD = 1.8) and 13.9 ± 2.1 Ma (MSWD = 2.3), respectively. At location 8, three fractured pebbles gave ages: (A) of 4.7 ± 1.0 Ma, (B) of 3.4 ± 0.8 Ma and (C) of 2.1 ± 1.8 Ma (with MSDWs of 2.0, 1.8 and 1.5, respectively). Since uncertainties on the age overlap these events likely occurred in a single tectonic phase around 3 Ma (Fig. 9).

To the south-east of the Chartreuse massif, a strike-slip fault plane from location 7 has been dated at 6.5 ± 0.6 Ma with a MSWD = 1.5 (Fig. 8). To the north of the Chartreuse massif, at location 12, a sample of the main reverse thrust, corresponding to the central Vercors thrust IIIa, has been dated to 13.6 ± 0.9 Ma with a MSWD = 2.0 (Fig. 8). To the north-western part of the Chartreuse massif, at location 14, related to thrust IIIb, a hundred-metre-long major thrust vein from a reverse fault plane has been sampled and dated at 11.1 ± 0.6 Ma (A1) and 10.5 ± 0.7 Ma (A2) with MSWD values of 1.5 and 1.9, respectively. The overlapping error bars of these two ages likely suggest a single fracturation event, but because they are from two different thin-sections, spots are not mutualized. To the south in the same major thrust, a reverse fault plane has been dated at location 15 (Fig. 8). Two ages have been obtained on this fault plane from the same thin-section: (A1) 16.6 ± 5.3 Ma (MSWD = 1.8) and (A2) 8.4 ± 1.5 Ma (MSWD = 0.99). Even though MSWD of A1 is acceptable, $^{238}U/^{206}Pb$ ratio only varies up to 25, which is reflected by the error bar but this age is taken as indicative. The "A2" age shows an

up to 150 $^{238}U/^{206}Pb$ ratio with a younger age that is still coherent with other location 14 ages (Fig. 8).

5.4.2.3. Vercors massif.
To the NE of the Vercors massif, in the footwall of the eastern Vercors thrust I (location 9, Fig. 7), five ages were obtained out of four strained pebbles thin-sections (Fig. 9). The oldest vein generation in location 9 (Fig. 9) is highlighted by 3 similar ages obtained in 3 different samples A (15.4 ± 1.1 Ma), B (15.4 ± 1.2 Ma) and 'C Rims' (15.2 ± 0.6 Ma) with good MSWDs (2.7, 1.6 and 1.3, respectively).

In order to decipher the relationship between vein opening and calcite U-Pb ages, a LA-ICPMS age map (Fig. 10c-d) was undertaken in one of the largest calcite filled-vein of blocky-calcite of sample C. This map exhibits two stages of calcite precipitation associated to opening of the 'generation 2' vein (C 'Rims': age of 15.2 ± 0.6 Ma and 'Core': age of 8.9 ± 0.7 Ma with a MSWD of 1.3 and 1.2, respectively).

On Fig. 10b, each spot of the age map has been numbered, boundaries have been traced based on LPNA and cathodoluminescence image (Fig. 10c), all data are available in Supplementary material 9. Thereafter, a ^{208}Pb cartography built by the interpolation of each analysed spot allows to delimit the boundary between the two compositional domains (Fig. 10d). While the edge presents dark shades in cathodoluminescence and high ^{208}Pb contents, the central part presents bright cathodoluminescence shades and low corresponding ^{208}Pb contents. Just below the dated area, an elemental cartography has been made (Fig. 11a). For ^{208}Pb and ^{57}Fe the sharp limit of the two generations calcite filled-vein is visible between the borders and the core. Whether it is for ^{208}Pb or for ^{57}Fe, the younger core generation is depleted ($0-5 \times 10^3$ and $1-2 \times 10^6$ CPS respectively) compared to the older rims' generation ($10-20 \times 10^3$ and $2-3 \times 10^6$ CPS respectively).

Concerning ^{238}U and ^{88}Sr, the distribution in these elements is heterogeneous with a core more depleted ($0-80 \times 10^3$ and $10-40 \times 10^6$ CPS respectively) than the rims ($0-160 \times 10^3$ and $10-40 \times 10^6$ CPS respectively) (Fig. 11b). The contents in ^{238}U and ^{88}Sr show anti-correlated patterns.

In addition, in the same location 9, another younger age (3.8 ± 0.2 Ma, MSWD = 1.2) was obtained from another sample (D). Further, five kilometers to the south, in the hanging-wall of eastern Vercors thrust I, at location 10, a strike-slip fault has been dated at 13.9 ± 0.8 Ma with a MSWD = 2.7 (Fig. 8). The MSWD value is highly improved (from 2.7 to 1.9) by removing the two spots close to 100 value of $^{238}U/^{206}Pb$ ratio, while the age and associated uncertainty only vary slightly (by −0.3 Ma and − 0.1 Ma, respectively).

In the southern part of the Vercors massif, at location 13, the major thrust IIIa was sampled (Fig. 7). The thrust gouge cement (sample B) and sigmoidal structures in the footwall (sample A, 20 cm close to the fault plane) have been dated (Fig. 8). The fault plane veins (sample B) returned an age of 7.7 ± 3.4 Ma and sigmoid veins (sample A) of 12.1 ± 0.4 Ma with a MSWD of 7.7 and 1.6, respectively. For the first age, the low number of spots (14) and the high MSWD are explained by the small size of dated calcite filled-veins (even with the reduced spot size) and the observation of clast contamination for some spots. This age is thus taken as an indicative estimate of the younger calcite generation. In contrast, sample A shows a well-constrained age with a good spread of $^{238}U/^{206}Pb$ ratios over 0 to 400 (Fig. 8).

At the western border of the Vercors massif, in the Bas-Dauphiné basin, at location 16, a fault plane related to Thrust V flexural slip (Fig. 7) gave two ages on different samples of (A) 8.9 ± 1.4 Ma and (B) 7.9 ± 2.4 Ma with MSWDs of 1.9 and 1.6, respectively (Fig. 8). Sample A shows a robust isochrone while sample B age has to be taken with caution because the correlation relies mainly on 2 points with relatively low $^{238}U/^{206}Pb$ ratios (25 and 70). The overlapping error bars of the two ages suggest a single fracturation event or tectonic phase.
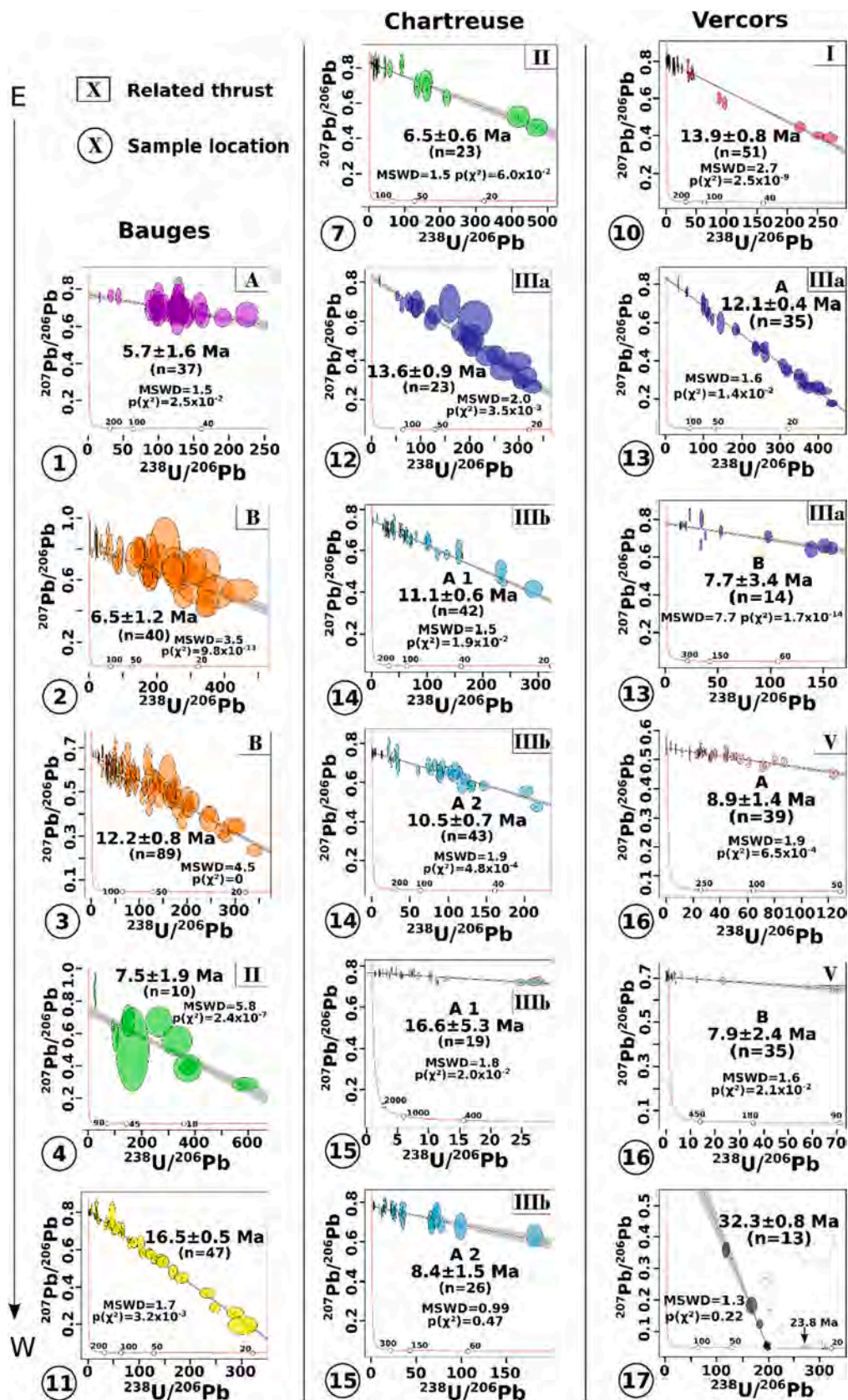
Fig. 8. Compilation of Tera-Wasserburg plot from reverse, normal and strike-slip fault planes. Numbers correspond to sample locations and colours refer to the sampled thrusts (Fig. 7).
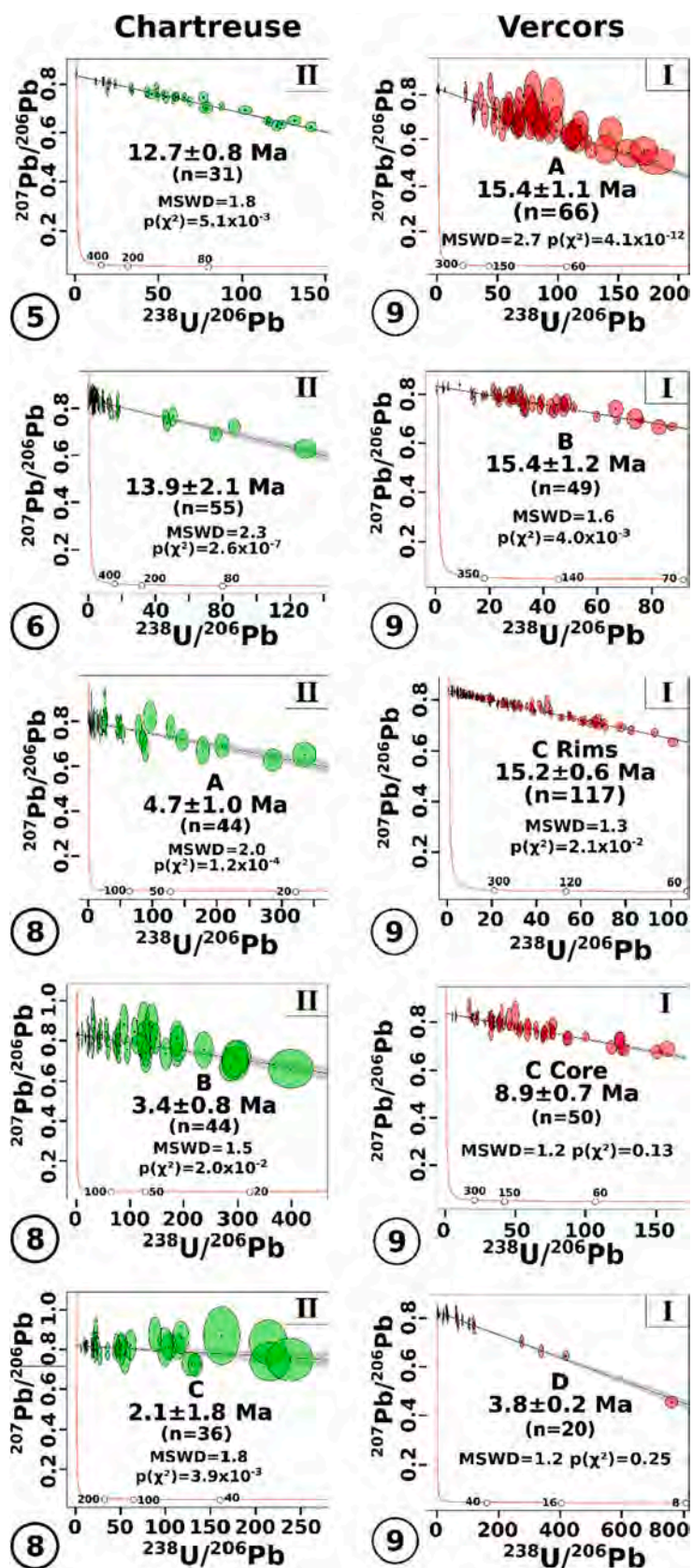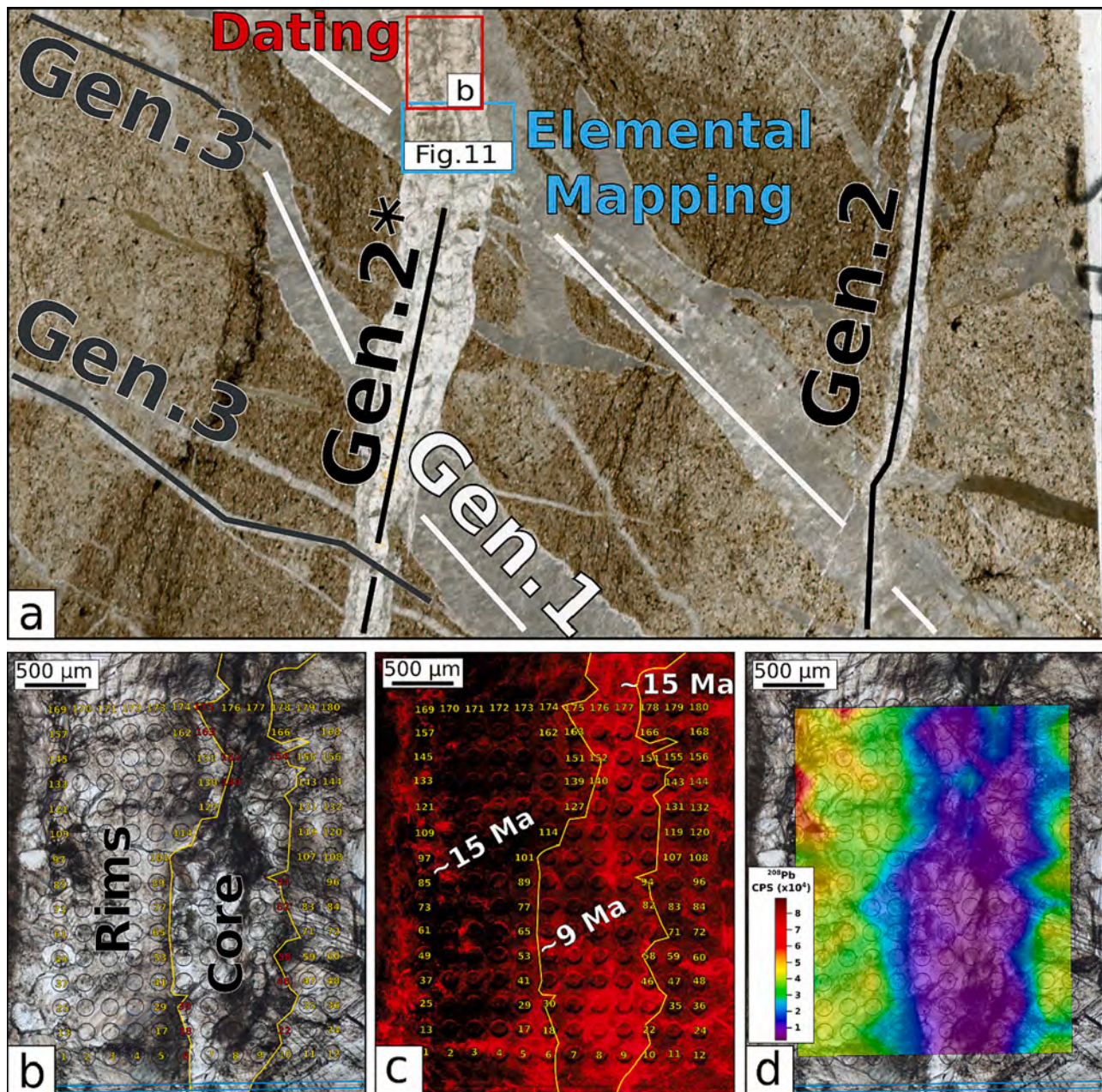
Fig. 9. Compilation of Tera-Wasserburg plots from fractured pebbles. Numbers correspond to sample locations, roman numbers and colours refer to the sampled thrusts (Fig. 5).

Fig. 10. (a) Thin-section of fractured pebble C from location 9 with cross relationships of calcite filled-veins. (b) Zoom on age cartography made on generation 2 filled veins, each spot corresponds to a U-Pb analysis. Red numbers correspond to straddles ousted spots. (c) Cathodoluminescence photography evidencing the dark borders of the generation 2 filled-veins dated at ~15 Ma and the lighter core dated at ~9 Ma (samples C in Fig. 9). (d) ^{208}Pb interpolation from age spots highlighting the 2 different generations inside the generation 2 filled veins. (For interpretation of the references to colour in this figure legend, the reader is referred to the web version of this article.)

6. Discussion

6.1. Limits for the application of U-Pb on calcite method, and sample selection

Calcite U-Pb geochronology is limited by its overall low U and Pb contents (~ <10 μg/g). Recent technical advances of LASER ablation coupled with mass spectrometers with improved sensitivity have allowed U-Pb dating of <1 cm calcite veins and to identify multiple generations (Roberts et al., 2021). Carbonate rocks usually show low uranium contents, typically 10 ppb to 10 ppm (e.g., Roberts et al., 2020). Calcites with an isotopic signature (δ^{13}C and δ^{18}O) close to their host-rock are thus interpreted as resulting from crystallization in a fluid at chemical equilibrium with the host-rock in a relatively closed system (small scale fluid flow) and thus generally resulting in a uranium-poor calcite (Fig. 5). It follows that, in our sample dataset, the majority of calcites falling within the "host-rock buffered" stable isotopic compositional domain (Fig. 5) does not have a sufficient uranium content to be datable. Conversely, the successfully dated calcites present a δ^{18}O signature different from their host-rock (±4‰ and more) with similar δ^{13}C signature. The origin of the uranium is thus supposed to result from the interaction of fluids with the underlying crystalline rocks, clay formations or minerals present in terrigenous formations like sandstones (e. g., Tartese et al., 2013). Thus, the supply of uranium to the calcite system is often facilitated by a relatively large-scale fluid flow with significant interactions with various kinds of host-rocks (Bilau et al., 2021).
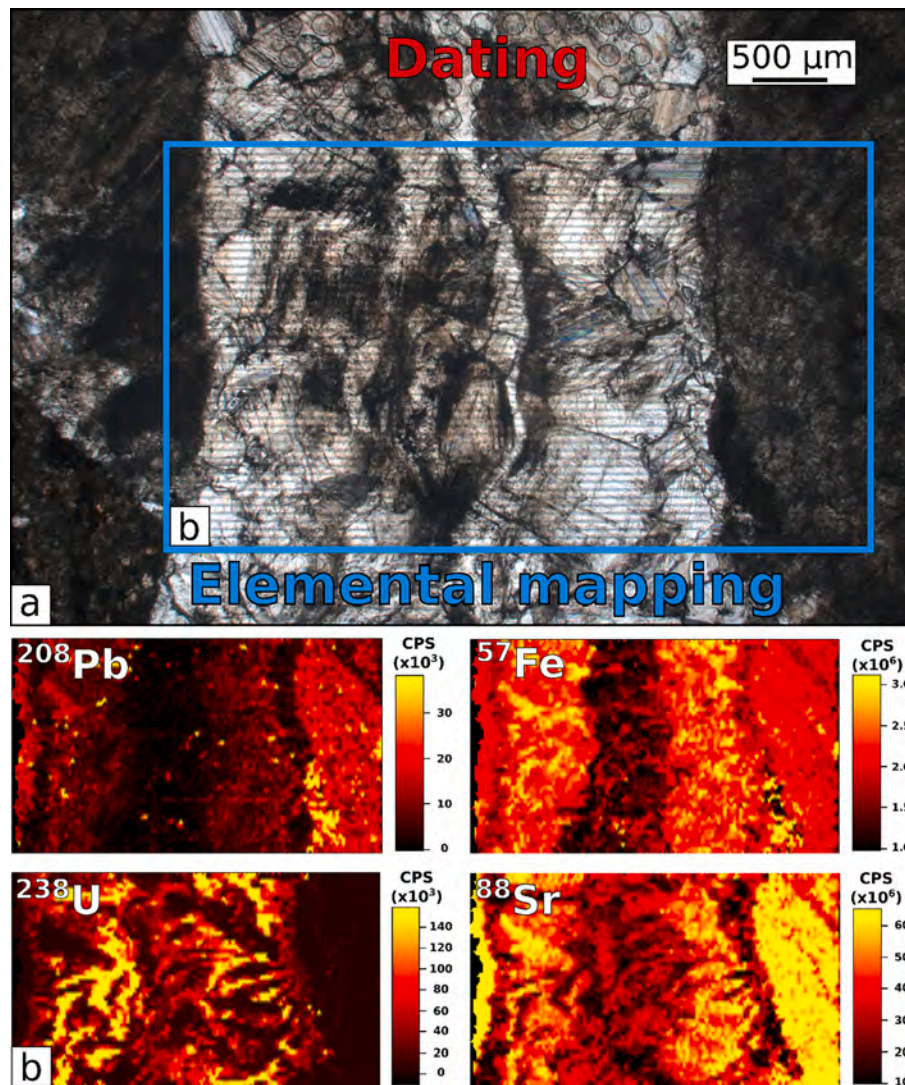
Fig. 11. (a) Zoom on elemental map zone. (b) Elemental mapping of the generation 2 calcite filled veins evidencing differences in various elemental contents in count per second: [208]Pb, [57]Fe, [238]U and [88]Sr.

Uranium incorporation in calcite is not only related to parental fluid uranium contents but also relies on calcite crystallization rates, which are a function of the opening fracture mode (Gabitov et al., 2014; Prajapati et al., 2018). Calcite texture can provide significant information to discriminate between the several opening fracture modes (Bons et al., 2012; Prajapati et al., 2018). Fibrous or elongated calcite crystals are observed in a continuous slow vein opening mode, whereas blocky calcite is related to a more spontaneous opening mode with a larger crystallization space. This consideration directly impacts the feasibility of U-Pb dating. Some progress on calcite U incorporation knowledge has been made by the study of natural samples and synthesized calcite (Weremeichik et al., 2017). For a slow crystallization speed rate of 0.001 $nm.s^{-1}$ the sharing ratio of U between fluid and calcite (K^U) is around 0.02 (no entrapment) whereas, for a rapid crystallization speed of 1 $nm.s^{-1}$ the K^U is 0.06 (100% entrapment) (Gabitov et al., 2014; Weremeichik et al., 2017). It follows that blocky calcite could entrap more U than fibrous calcite making it more suitable for dating. Fibrous calcite crystallization related to *syn*-kinematic continuous slow opening process and usually related to the beginning of the fracturation (Prajapati et al., 2018) seems to incorporate less U. In our study, we confirm that, in terms of their stable isotopic composition, fibrous calcite stands close to their host-rock signature. Although almost all the calcites (6/8) in the host-rock domain were unsuccessful candidates for U-Pb dating,

one of these was dated (SIMS analyse from sample D at location 9, with 1.3‰ δ^{13}C and − 5.6‰ δ^{18}O, Fig. 5). It follows that nearly all of the low $\delta^{18}O_{calcite}$ ratio ($< −6$‰) calcites (18/19) appear to be suitable for U-Pb dating. Furthermore, oxidation state of uranium is also important, oxidised uranium is mobile in fluid while reduced uranium is easily incorporated in calcite structure (Gabitov et al., 2021). The following process can be imagined, oxidating meteoric fluid deeply percolating, interacting with crystalline rocks and becomes enriched in δ^{18}O and U then is mobilized by fault networks and become reduced and crystallize calcite at the same time.

In conclusion, in a carbonate context similar to the subalpine massifs, a blocky calcite with a stable isotope signature different from the host-rock seems to be more suitable candidate for U-Pb calcite dating than those that equilibrated with the host-rock, and especially the fibrous calcite. This indication should thus be taken in consideration for future sample selection.

6.2. Significance of U-Pb calcite ages

The main question that we address here, following recent works on this theme (e.g., Roberts et al., 2021), is how can we interpret the obtained U-Pb calcite ages?

Based on either experimental or natural examples, it is shown that

calcite crystallization is a rapid process. Natural example of fault-related veins dated by U-Th of calcite suggests a crystallization speed rate of ~0.03 to 0.80 mm.ka^{-1} (Uysal et al., 2007, 2011; Williams et al., 2019). The calcite crystallization process can thus be considered as instantaneous in sight of the geological age and precision we are looking for to reconstruct the deformation sequence of a fold and thrust belt on millions of years' scale. In addition to the opening rate, the calcite texture is also a function of the fluid source and rugosity of the pore's wall (Nollet et al., 2009). Fibrous calcite is more likely to develop in a local pore-fluid derived fluid with a slow opening rate whereas elongated blocky calcite is more likely to grow with smooth vein walls, an external fluid source and a related higher opening rate as in a single fracturation event (Nollet et al., 2009). At location 9, the age of 15 Ma is observed on three different pebbles from Miocene conglomerate, which seems to indicate that the porosity was filled within a period of time shorter than the uncertainty on the ages (~ < 0.5 to 1 Ma). With the assumption that the porosity is not left empty, the age of crystallization can be considered as equivalent to the age of fracturing. Furthermore, pebble elongation and calcite cemented offset are tectonic markers indicating a post-depositional deformation linked to thrust activity. An important part of the field and petrographic analysis is thus to characterize each cogenetic calcite generation in order to sample and date them independently. Within a single generation, even if a calcite shows a growth zoning, the age between the edge and the core of a calcite grain (considered as part of the same crystallization event) is the same at the sight of our 0.1 Ma analytical precision (e.g., Bilau et al., 2021). In addition, it is not uncommon to observe calcite filled-veins with residual porosity (partially-open, Prajapati et al., 2018) in the form of a void and the measured age is the same independently of the proximity to the residual porosity.

Now that the calcite crystallization is considered as a fracturation age, is this age robust or may it be reset by any further deformation or fluid flow events? The common idea we have about calcite is that it is not a very resistant mineral, and that it is highly sensitive to fluid circulation (Lamy-Chappuis et al., 2016). As opposed to the (U-Th)/He method, uranium replaces calcium in the calcite structure (Gabitov et al., 2021) and in the absence of any recrystallization evidence, that could be observed in thin section, it has a stable lattice position in natural calcite, in uranyl form, U(VI), (Reeder et al., 2000; Kelly et al., 2003; Ortega et al., 2005) but Gabitov et al. (2021) shows that tetravalent U(IV) uptakes by calcite is four orders of magnitude higher that oxidised U(VI), (Rasbury and Cole, 2009; Gabitov et al., 2021). In the absence of any dissolution or recrystallization features, the U-Pb system in calcite seem to remain in a closed system. In calcite, chemical zoning profiles alike zircon has not been observed. At the corresponding temperature range to calcite growth, solid diffusion seems too slow and should be considered null. Therefore, a reset of calcite age in response to diffusion is unlikely. However, the circulation of aggressive fluids will lead to a complete dissolution of calcite and possible reprecipitation, anyway such features can be observed in cathodoluminescence and are not present in our samples. Moreover, given this solid behaviour of U-Pb system in calcite once, in order to obtain a robust isochrone from a Tera-Wasserburg plot, one has to recognize and date a single synchronous generation. Otherwise, it is not possible to undertake any linear regression with all the dataset, as the dated spots will result in a significant scattering. The assumption underlying the use of this diagram is the presence of a cogenetic generation (e.g., Roberts and Holdsworth, 2022). In Fig. 10, the age map highlights that a single age, reflected by a homogeneous composition for the whole calcite generation, is obtained. The demarcation between the two age domains is sharp without any apparent mixing of ages at the <10 μm scale. Furthermore, the older 15 Ma calcite is well preserved, even if the vein was re-opened under the same stress system (similar vein orientation). The fact that a 15 Ma age is also obtained in two other pebbles confirms that the reopening of the vein did not alter it. It is thus likely that a new porosity was created and was rapidly sealed by fluids and calcite precipitation while the older

calcite remained intact.

6.3. The nature of fluids during deformation, and insights for fluid-rock interaction and burial

Host-rock $\delta^{18}O$ and $\delta^{13}C$ signature leads to define a domain so-called «host-rock buffered domain» to the analysed veins. Calcites from this domain are interpreted as resulting from the crystallization of a fluid with a low fluid/rock ratio in equilibrium with the host-rock. Calcites with a lower $\delta^{18}O$ value are suggested to fall in an 'unbuffered domain' relative to the host-rock composition. All together, these analyses define the "unbuffered domain" of our vein dataset. Calcites from this domain are interpreted as resulting from the crystallization of a fluid with a high fluid/rock ratio, which did not allow it to fully equilibrate with the vein host-rock. Clumped isotopes may retain the nature of percolating fluids and paleo-temperatures, which can be used to constrain burial dynamics (Smeraglia et al., 2019; Curzi et al., 2021; Looser et al., 2021; Smeraglia et al., 2021). Moss (1992) was the first to bring some burial temperature constrains using vitrinite reflectance (R_o) in Subalpine massifs. Cretaceous units have low R_o (<0.5%), which gave a burial temperature of 40–90 °C (Fig. 12), according to Basin%R_o and Easy%R_o (vitrinite to °C conversion model, Nielsen et al., 2017).

However, these estimates can be affected by the exposure time at a given temperature, so deduced temperatures from Moss (1992) may be indicative. Jurassic units have higher R_o from 0.8% to 1.25%, corresponding to significantly higher temperatures (~135 °C to ~180 °C). Furthermore, for the same geologic units, higher R_o values have been observed for the north Chartreuse than for the south Vercors and also inside each Subalpine massif, with increasing values towards the east. The N-S gradient has been interpreted as related to an earlier and more significant burial in the north, while W-E gradient is related to a thicker tectonic load at the front of the ECM (e.g., Bellahsen et al., 2014). Moss (1992) suggested that the Vercors and Chartreuse Subalpine massifs underwent a rather limited burial (40–80 °C for Hauterivian units and 100–160 °C for Upper to Middle Jurassic units) for a short duration (<10 Ma).

These rather high temperatures obtained for the eastern part of Vercors compare well to Raman Spectrometry of Carbonaceous Material (RSCM) conducted on ECM Mesozoic cover by Bellanger et al. (2015) who obtained a uniform maximum temperature of ~330 °C decreasing to <200 °C in neighbouring east Vercors Jurassic limestones.

These recorded T_{max} at the base of the ECM Mesozoic sedimentary cover are consistent with a thickness of 8–11 km of tectonic nappes above ECMs (Philippe et al., 1998; Bellanger et al., 2015). Δ_{47} temperatures related to *syn*-fracturation calcite obtained in this paper complement this rather significant increase in burial temperatures from west to east. Δ_{47} temperatures increase from 54 °C in the central Vercors thrust (location 13, Fig. 12) to 149 °C in eastern Vercors thrust footwall (location 9, Fig. 12). The determination of the calcite crystallization temperature by an independent method combined to calcite $\delta^{18}O$ signature allows the calculation of $\delta^{18}O_{fluid}$ signature with Kim and O'Neil (1997) equation (Table 1, Fig. 13). These two fluid isotopic signatures are interpreted as distinct fluid sources:

- Fluid composition in central Vercors corresponds to a colder fluid with a $\delta^{18}O_{fluid}$ composition of 5‰ SMOW compatible with a heated meteoric fluid which slightly interacted with carbonate rocks (Hoefs, 2021).

- Fluid composition and paleotemperature in eastern Vercors are indicative of hydrothermal fluids which interacted with crystalline rocks and/or metamorphic fluids (e.g., Brigaud et al., 2020).

At central Vercors (location 13), the sealing calcite $\delta^{18}O$ signature plots within the host-rock domain (Fig. 5) with a crystallization temperature of 54 °C, the resulting parent fluid is about 5‰ SMOW. This positive value could result from an interaction (dissolution) with the Urgonian host rock. The fault gouge cross-cutting veins have a low $\delta^{18}O_{calcite}$ value (−9‰), highly depleted compared to the host-rock
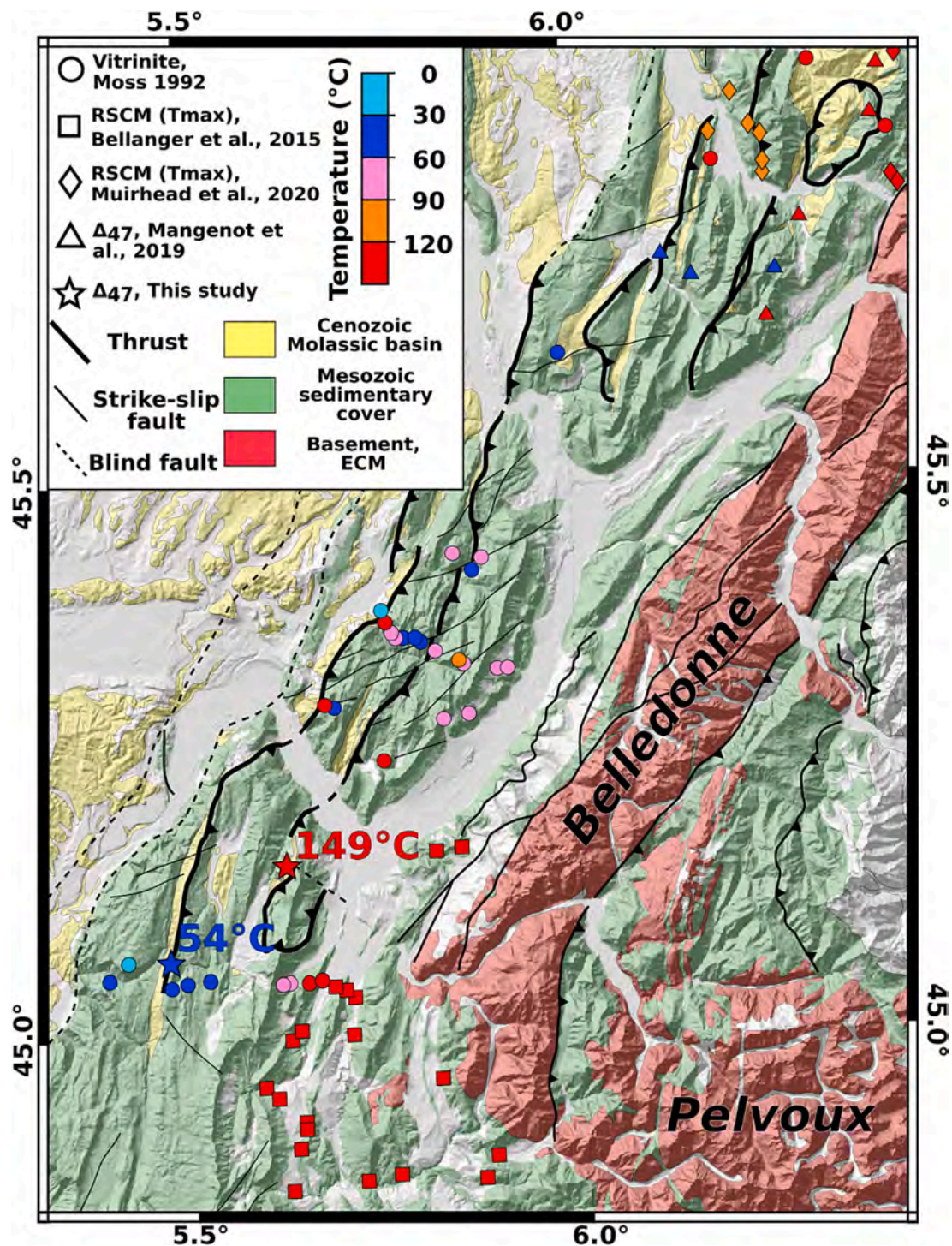
Fig. 12. Simplified map of the studied zone with a compilation of the temperature estimation (Vitrinite, RSCM (T$_{max}$) and Δ_{47}). The Δ_{47} from this study are indicated by a star.

signature, which is interpreted to result from a cold (<60 °C) meteoric fluid.

Based on these arguments, the recorded crystallization temperature of 54 °C (Table 1, Fig. 13) is interpreted as resulting from a surface or basin-derived fluid that equilibrated with surrounding rocks at shallow ~1-2 km depth. This shallow burial depth can be explained by a moderate underthrusting of the molasse. In eastern Vercors, the estimated temperature is of 149 °C. This elevated temperature is coherent with the observation of a more ductile deformation style and with similar temperature estimates obtained by independent methods (vitrinite

reflectance and RSCM, Fig. 12). Based on these data and taking into account a geothermal gradient of 25 to 35 °C/km, the ~150 °C temperature can be related to a maximum burial depth of 4-6 km. The significant difference in temperature (~100 °C) recorded between eastern and central Vercors highlights a marked increase of the tectonic thrust stack in front of the ECM. Because the fracturation and the vein opening are supposed to occur at the burial peak, this high recorded temperature is interpreted as a crystallization temperature with little influence of solid-state reordering (Henkes et al., 2014; Stolper and Eiler, 2015; Mangenot et al., 2019). This temperature is close to the closure
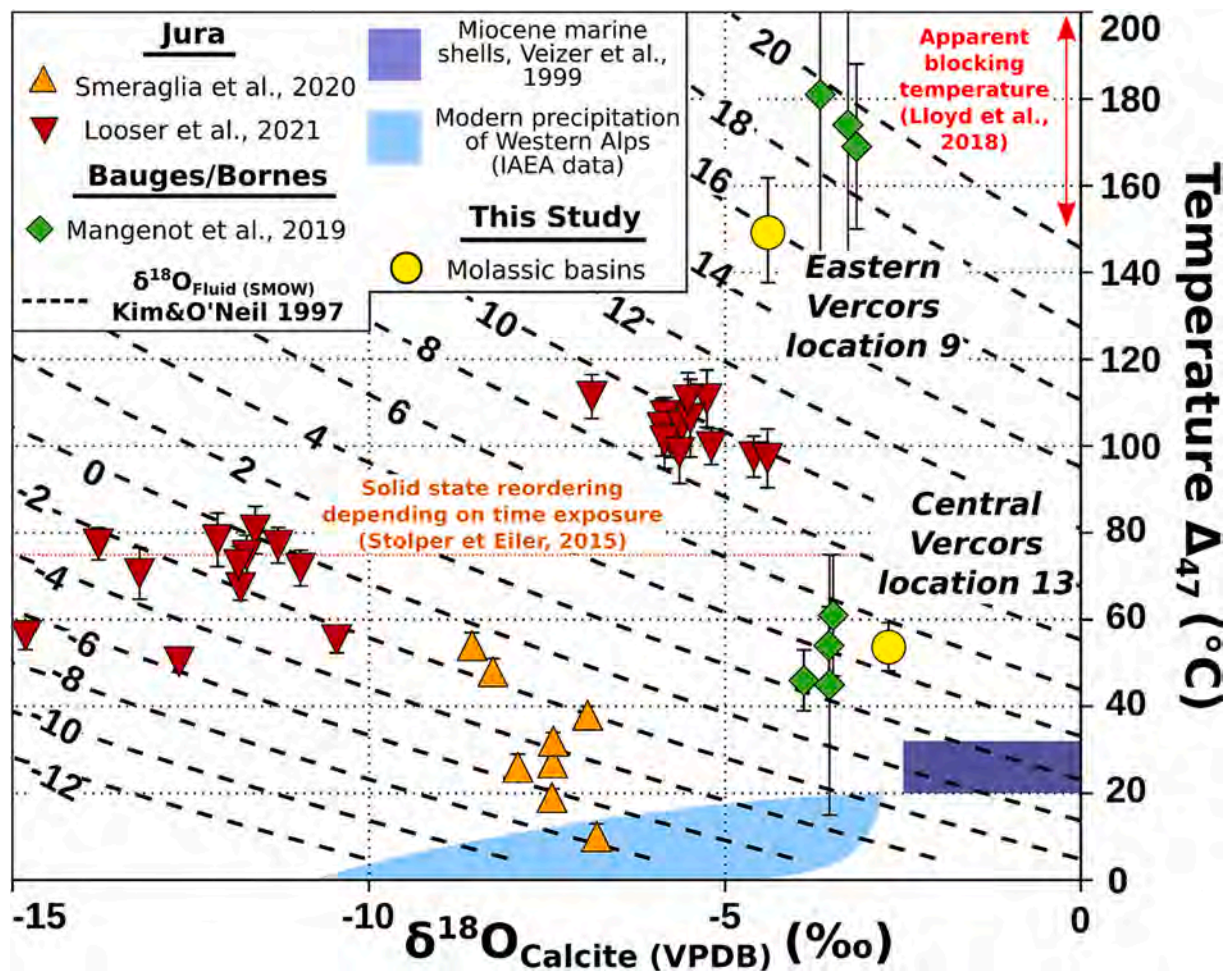
Fig. 13. Recalculated Subalpine and Jura Δ_{47} temperature versus $\delta^{18}O_{Calcite\ (VPDB)}$ and calculated $\delta^{18}O_{Fluid\ (SMOW)}$ in dashed lines (Kim and O'Neil, 1997). Fields are based on literature: mollusc shells compiled in (Veizer et al., 1999) are supposed in equilibrium with marine water temperatures, following Mangenot et al. (2019); precipitation field relies on IAEA data of Wiser program, https://nucleus.iaea.org/wiser/index.aspx, $\delta^{18}O_{Fluid\ (SMOW)}$ and Air temperatures from Malaussene, Carpentras, Draix and Thonon-les-Bains.

temperature of the U-Pb system in calcite (150°-200 °C, Lloyd et al., 2018) so the calcite could have been exposed to higher temperatures (deeper burial) without being recorded. Consequently, the derived fluid signature can be interpreted as a maximum value of $\delta^{18}O_{fluid}$. The recalculation of the fluid signature at equilibrium at the Δ_{47} temperature of 149 °C leads to a minimum ratio of 15.9 ‰. This high value, which can only be associated with highly enriched fluids, may also be the result of diffusion in the solid state and would therefore be a maximum value.

Towards the north, the Bauges and Bornes massifs show a similar increase in maximum recorded temperatures estimated from RSCM data (Muirhead et al., 2020), Δ_{47} on host-rock, and illite crystallinity (Mangenot et al., 2019). These data show a significant variation of maximum burial temperature (from <70 °C in the west to 300 °C in the east of these massifs). The difference in maximum temperature between the Bauges-Bornes and Vercors massifs, and from west to east within these massifs, is interpreted as resulting from a variation in the structural nappe stack thickness.

6.4. Relationship of the thrust propagation sequence with molassic basins emplacement

Sedimentation in the molassic basins in this zone is bracketed in the range ~ 20–15 Ma (Kalifi et al., 2021). These authors suggested that subsidence occurred in relation to the activation of the thrust sequence (i.e., 'tectonic subsidence'). Along our dated transect within the

Subalpine massifs, the age of sedimentation suggested by Sr isotopic ratios clusters mostly between 18 and 16 Ma (Fig. 14; Kalifi et al., 2021). The comparison of thrust U-Pb calcite ages shows a good fit with the basin sediment ages, and suggests that thrust activation shortly followed the end of sedimentation in each sector. However, The U-Pb calcite ages obtained in this study are mostly younger (15 Ma maximum) than the molasse sedimentation ages in the Subalpine massifs, which suggests that the timing of fault development is decoupled from that of sedimentation. It follows that the mechanism of frontal basin opening is dominated either by a more eastern fault (located to the east of the Belledonne ECM), or by eustatic variation and/or regional subsidence instead of local parameters like in-sequence thrust propagation within the Subalpine domain. It seems that there is a link between the activation of the central Vercors and eastern Chartreuse thrusts (dated at ~12 Ma in this study) and molasse deposition at the front of Subalpine massifs in the Bresse basin, where sedimentation is restricted to 12 to ~8.2 Ma (Kalifi et al., 2021). The perfect match of activity of the Bresse foreland basin with the central Vercors thrust is suggestive of a tectonic control of this phase of basin subsidence.

6.5. Evolution of the stress field and proposed tectonic model

The combination of paleo-stress reconstructions and U-Pb dating undertaken on the same calcite sample allows to decipher the evolution of stress through time in a given geological area. All the dated tensors
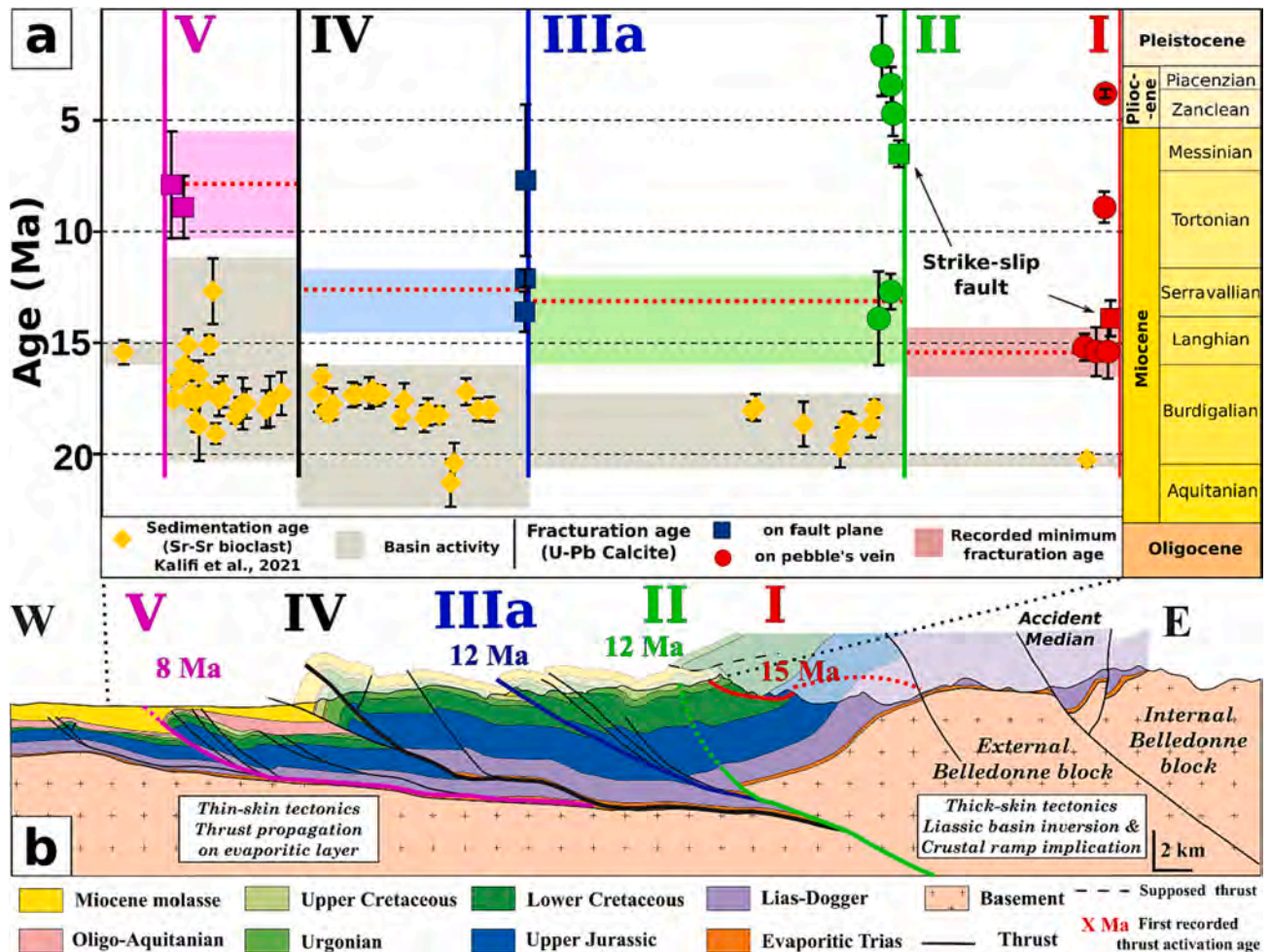
Fig. 14. (a) Timeline of the development of the thrust sequence on a NW-SE profile and comparison with the sedimentation ages of molassic basins. (b) W-E Cross-section, modified from Kalifi et al. (2021) with major thrust activation. Fault names related to roman numerals are described in Fig. 1 caption. See Supplementary material 4 for a zoomed cross-section of the eastern Vercors side.

that were obtained in Fig. 6 (i.e., all locations except 17) are shown in the compilation (Fig. 15) featuring the tectonic evolution of the Alpine foreland constrained by U-Pb ages on calcite. The fault data inversions carried out in this study show a good consistency of results at the regional scale. Two main trends are observed for the compressional axes: *E*-W to NW-SE and NW-SE. In the overthrust limestone deformed cover (locations 1 to 17), homogeneous datasets, low dispersion of the P-B-T axes and internal friction angles close to the average value accepted in the rocks (~30°; except for locations 2′, 4, 11 and 17 where internal friction angles lower than 20° are obtained) show a good reliability of results, even in case of a small number of data (<8 data, location 17). These results appear to be consistent with the geometry of the main tectonic faults that were studied. On Fig. 15, paleostress results displayed for the oldest recorded calcite U-Pb calcite ages, can be depicted in three stages corresponding to three distinct states of stress:

(1) During stage 1, ranging between 17 and 14 Ma the stress regimes of Bauges and Vercors massifs were different. In the Bauges massif, a N*E*-SW compressive axis is recorded and interpreted as resulting from a transpressional side effect of deformation during early stages of deformation of the Bornes-Bauges and Jura massifs, in response to exhumation of Aiguilles Rouges and Mont Blanc ECMs (e.g., Boutoux et al., 2016; Rolland and Rossi, 2016), while ECM exhumation remained low at ~17 Ma in the Belledonne massif (Girault et al., 2022). In the meantime, NW-SE compression is recorded in the Vercors-Chartreuse massif and is

attributed to the first signs of Alpine compressional tectonic activity in these subalpine massifs.

(2) During stage 2, from 14 Ma to 10 Ma, Bauges and northern Chartreuse show NE-SW and NW-SE compressional axes, respectively. The influence of more significant displacements in the Jura massif compared to the subalpine massifs could induce strain accumulation in the limit of these massifs accommodated as local strike-slip deformation regime observed in southern Bauges. In contrast, the northern Chartreuse massif underwent a more E-W compression in relation to the thrust geometry, and the absence of evaporites inducing less basal decoupling. At the same time, a similar pure E-W orientation is observed in Vercors and southern Chartreuse massifs. We propose that the rapid activation of numerous frontal thrusts in a short time period (~1 Ma) at ~12 Ma is related to a more rapid exhumation of the Belledonne MCE indicated by ZHe ages (Girault et al., 2022). We suggest that the rapid propagation of the deformation in the Subalpine Massifs is controlled by the activation of a blind crustal-scale ramp located at the front of Belledonne MCE (Fig. 14). This change in stress direction could result from the structural anisotropy of the region, and is especially ascribed to the reactivation of N-S inherited crustal structures. The N-S sub-vertical anisotropy corresponds to the East Variscan shear zone (e.g., Corsini and Rolland, 2009; Simonetti et al., 2020) in the basement along the MCE, the Jurassic extensional faults (e.g., Lemoine et al., 1986) and the Oligocene extensional faults like the one dated at 32 and
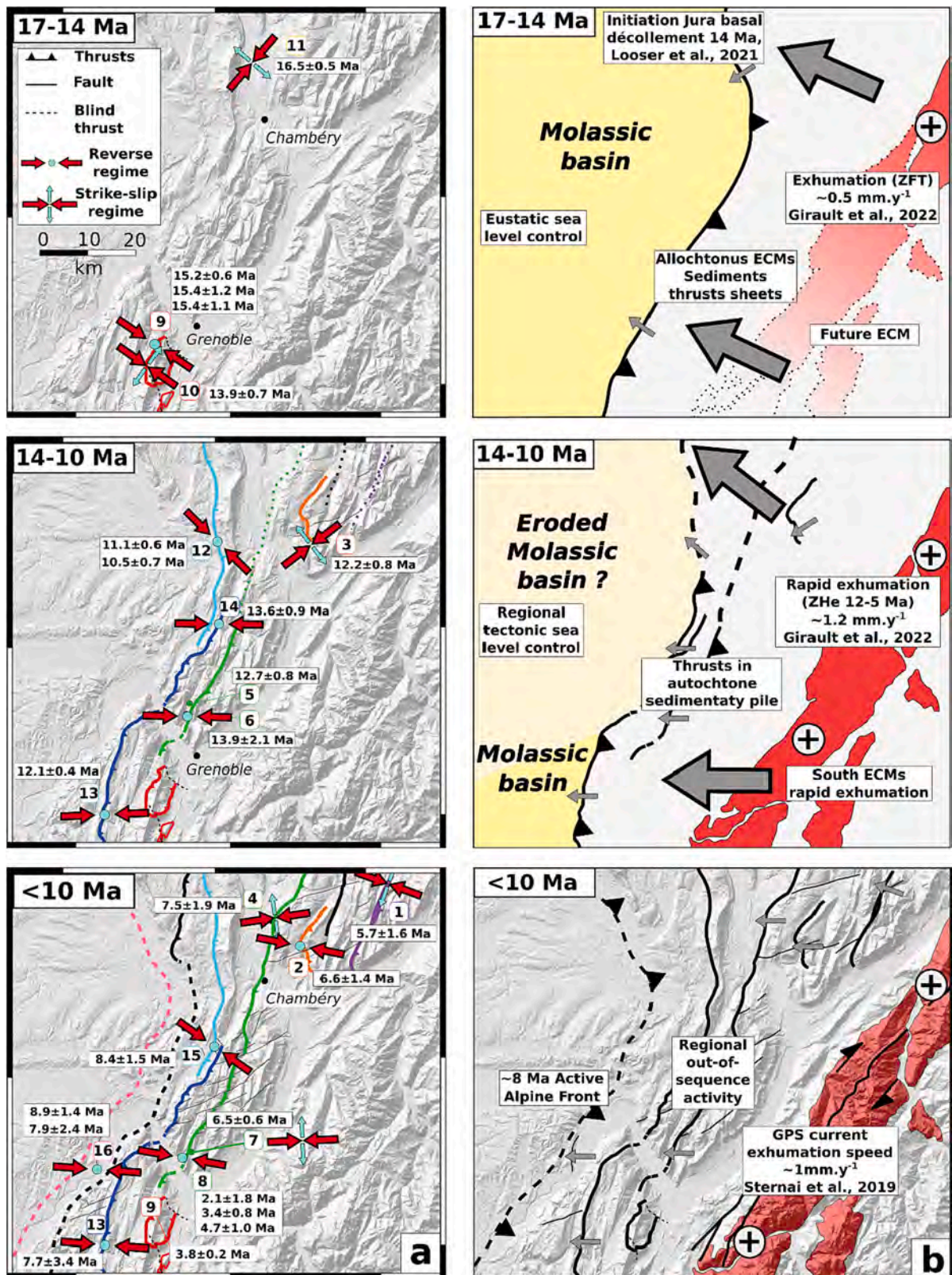
Fig. 15. Sketch depicting the evolution of strain context through time, the involved faults and related ECM exhumation. Activation of the different thrusts is inferred by the first age recorded for each fault. Small grey arrows are local data derived stress orientation while big grey arrows are regional interpreted stress orientation. Black cross in a grey circle are exhuming zones.

24 Ma (location 17, Fig. 8). These inherited faults have clearly controlled the localization of major thrust as highlighted by the eastern Vercors structure (e.g., Fig. 14b, Schori et al., 2021).

(3) Since 10 Ma, ECMs have been uplifted at a somehow constant rate, as suggested by a similar magnitude of exhumation rates (about 1 mm.yr^{-1}) deduced from thermochronology (Girault et al., 2022) and vertical motions recorded by GPS data (Sternai et al., 2019). A fairly uniform *E*-W stress field is recorded from Bauges to south Vercors with the activation of the Western Subalpine thrust and multiple "hors-sequence" reactivation of the thrusts in a dominant strike-slip context until present (Rolland et al., 2022).

6.6. Timing of fold-and-thrust belt propagation

The new U-Pb calcite ages obtained in this study allow to constrain the timing of the thrust propagation sequence in the Subalpine massifs. Based on the distribution of the different ages obtained from the different thrusts (Fig. 14), and the structural relationships (based on Deville, 2021; Kalifi et al., 2021 and references therein), it appears that four major thrusts have been activated from east to west:

(1) The most eastern thrust in the Vercors massif was activated around 15 Ma in a NW-SE compressional context.

(2) To the west, in-sequence thrust activation propagation occurred with the activation of the central Vercors thrust and *E*-W shortening around 12 Ma. It appears from structural relationships that this fault system is in continuity with the eastern Chartreuse thrust, and that its southward propagation in Vercors is split into two main different faults (the II and IIIa thrusts, as shown on Fig. 14). At this stage, based on the basement offset in the rooted trust we assume that the deformation is mostly in a thick-skin mode as the deformation front is not significantly transferred into the evaporitic layer at the base of the sediment cover. In contrast, this phase correlates with an acceleration of the Belledonne ECM, through the activation of a crustal ramp, rooted directly west of the ECM.

(3) A transfer of this motion occurred around 10 Ma on the western Vercors-Chartreuse thrusts (e.g., west Vercors thrust, Fig. 15). This rapid propagation of thrusts is supposed to be related to the transmission of stress by the Triassic decoupling evaporitic layer which marks a transition from thick-skin tectonics to a more thin-skin tectonic mode. However, based on geological cross-section (Fig. 14) it seems that the flat decoupling layer always branch on the same transcrustal fault at the base of Belledonne ECM.

(4) A final in-sequence activation of the mostly blind Western Subalpine thrust is constrained at 7–9 Ma, still in agreement with a propagation of the decoupling layer on basal evaporites. However, at massif scale, it appears that this front progressed more to the west of Vercors than of Chartreuse, probably due to the lack of evaporites below this later massif and a location of the basal décollement in Lias-Dogger marly shales (Deville, 2021). As a result, we interpret the development of NE-SW dextral faults of southern Chartreuse as a result of this differential propagation of the active front between the two massifs. Indeed, the dextral lineaments clearly offset the 10–12 Ma thrusts, and thus could be correlated with this ~7–9 Ma final propagation event. The propagation of the deformations towards the foreland is likely to have induced an uplift of the most internal subalpine massif and could therefore explain a more significant erosion and exhumation (about 4–6 km) of these domains.

After this fold-and-thrust propagation that occurred between 15 and 7 Ma, widespread and diffuse "out-of-sequence" reactivation occurred in the whole subalpine massifs. Widespread reactivations of internal thrusts may result from the locking of thrust propagation to the west.

This phase is highlighted by the re-opening of veins in the eastern Vercors thrust around 9 Ma (Fig. 9). Younger deformation (e.g., 6.5 ± 0.6 Ma at location 7) is recorded by a widespread strike-slip activity always in an E-W (σ1) compressional context which indicates a permutation of σ2 and σ3 stress axes. Since ~6 Ma, this evolution towards a more strike-slip dominated regime in a similar context as nowadays may be caused by a modification of the regional strain-field that could be ascribed to the Apulian late rotation (e.g., Collombet et al., 2002; Rolland et al., 2012; Walpersdorf et al., 2018).

7. Conclusion

Through the example of the subalpine fold-and-thrust belt, this study establishes a multi-technique methodology based on fault data inversion, conventional and clumped isotopes and U-Pb calcite dating in order to provide a detailed comprehension of the Tertiary tectonic structuration of the frontal part of the western Subalpine foreland. These combined approaches on calcite have allowed to constrain the timing of the fold and thrust belt propagation, which occurred in an 'in-sequence' mode between 15 Ma and 7 Ma. This propagation is dominated by a phase of thick-skin tectonics, highlighted by the activation of central Vercors and eastern Chartreuse thrusts at 12 Ma. This activation is correlated to the acceleration of Belledonne ECM exhumation, and it follows, based on structural relationships, that the foreland thrusts were rooted in a crustal-scale ramp below the ECM. The reorientation of the stress field from NW-SE to E-W compression since 12 Ma is ascribed to the N-S orientation of the crustal anisotropies, which originate from the Variscan, Tethyan, and early Alpine tectonic stages. In this work, the U-Pb dating of preserved Oligocene calcites at 32 Ma and ~ 24 Ma agree with the reactivation of N-S faults within the Subalpine massifs. After 10 Ma, and until 7 Ma, the most frontal (western) thrusts have been activated due to the propagation of a décollement on the evaporites of the basement – cover interface. This phase induced a differential motion of the Vercors with respect to the (evaporites-poor) Chartreuse massifs, which explains the development of cross-cutting dextral strike-slip faults in the latter massif. Finally, a further out-of-sequence reactivation is recorded from 6 Ma to 2 Ma, and is still ongoing from the seismic records, that is related to a more regional transition probably related to Apulian rotation. In this well-constrained tectonic context, stable isotope analysis brings some complementary information about the origin of fluids and the fluid-rock interaction history, providing independent constraints on the depth and connectivity of the fault systems. Most of the successfully dated calcites show a depleted $\delta^{18}O_{calcite}$ signature compared to their host-rock, which indicates an external fluid source, explaining a slight enrichment in U. This fluid source, recalculated with clumped isotopes, is similar to surface meteoric fluids that interacted with the host-rock during deformation. It is also observed that most successful dates are obtained in a blocky calcite, which results from higher fluid/rock ratios, while the fibrous calcite exhibits lower U contents and is isotopically close to the host-rock. Clumped isotope analysis highlights a strong temperature gradient from west (~50 °C) to east (≥150 °C), in agreement with vitrinite and RSCM data, coherent with an increase of burial from 2 to 4–6 km. This burial is related to an increase of the underthrusting below the Alpine frontal thrusts.

Declaration of Competing Interest

The authors declare that they have no known competing financial interests or personal relationships that could have appeared to influence the work reported in this paper.

Data availability

Data will be made available on request.

Acknowledgements

Appendix A. Supplementary data

Supplementary data to this article can be found online at https://doi.org/10.1016/j.earscirev.2022.104270.

References

Andrieu, S., Brigaud, B., Barbarand, J., Lasseur, E., 2018. The complex diagenetic history of discontinuities in shallow-marine carbonate rocks: new insights from high-resolution ion microprobe investigation of δ 18 O and δ 13 C of early cements. Sedimentology 65, 360–399. https://doi.org/10.1111/sed.12384.

Angelier, J., Mechler, P., 1977. Sur Une methode graphique de recherche des contraintes principales egalement utilisables en tectonique et en seismologie : la methode des diedres droits. Bull. Soc. Géol. France S7-XIX, 1309–1318. https://doi.org/10.2113/gssgfbull.S7-XIX.6.1309.

Barfety, J.-C., Gidon, M., 1996. La structure des Collines bordières du Grésivaudan et des secteurs adjacents, à l'est de Grenoble (Isère, France). Géologie alpine 72, 5–22.

Beaudoin, N., Lacombe, O., Roberts, N.M.W., Koehn, D., 2018. U-Pb dating of calcite veins reveals complex stress evolution and thrust sequence in the Bighorn Basin, Wyoming, USA. Geology 46, 1015–1018. https://doi.org/10.1130/G45379.1.

Bellahsen, N., Mouthereau, F., Boutoux, A., Bellanger, M., Lacombe, O., Jolivet, L., Rolland, Y., 2014. Collision kinematics in the western external Alps. Tectonics 33, 1055–1088.

Bellanger, M., Augier, R., Bellahsen, N., Jolivet, L., Monié, P., Baudin, T., Beyssac, O., 2015. Shortening of the European Dauphinois margin (Oisans Massif, Western Alps): new insights from RSCM maximum temperature estimates and 40Ar/39Ar in situ dating. J. Geodyn. 83, 37–64. https://doi.org/10.1016/j.jog.2014.09.004.

Bilau, A., Rolland, Y., Schwartz, S., Godeau, N., Guihou, A., Deschamps, P., Brigaud, B., Noret, A., Dumont, T., Gautheron, C., 2021. Extensional reactivation of the Penninic frontal thrust 3 Myr ago as evidenced by U-Pb dating on calcite in fault zone cataclasite. Solid Earth 12, 237–251. https://doi.org/10.5194/se-12-237-2021.

Bonifacie, M., Calmels, D., Eiler, J.M., Horita, J., Chaduteau, C., Vasconcelos, C., Agrinier, P., Katz, A., Passey, B.H., Ferry, J.M., Bourrand, J.-J., 2017. Calibration of the dolomite clumped isotope thermometer from 25 to 350 °C, and implications for a universal calibration for all (Ca, Mg, Fe)CO3 carbonates. Geochim. Cosmochim. Acta 200, 255–279. https://doi.org/10.1016/j.gca.2016.11.028.

Bons, P.D., Elburg, M.A., Gomez-Rivas, E., 2012. A review of the formation of tectonic veins and their microstructures. J. Struct. Geol. 43, 33–62. https://doi.org/10.1016/j.jsg.2012.07.005.

Boutoux, A., Bellahsen, N., Nanni, U., Pik, R., Verlaguet, A., Rolland, Y., Lacombe, O., 2016. Thermal and structural evolution of the external Western Alps: insights from (U–Th–Sm)/He thermochronology and RSCM thermometry in the Aiguilles Rouges/Mont Blanc massifs. Tectonophysics 683, 109–123.

Brand, W.A., Assonov, S.S., Coplen, T.B., 2010. Correction for the 17O interference in δ(13C) measurements when analyzing CO2 with stable isotope mass spectrometry (IUPAC Technical Report). Pure Appl. Chem. 82, 1719–1733. https://doi.org/10.1351/PAC-REP-09-01-05.

Brigaud, B., Bonifacie, M., Pagel, M., Blaise, T., Calmels, D., Haurine, F., Landrein, P., 2020. Past hot fluid flows in limestones detected by Δ47–(U–Pb) and not recorded by other geothermometers. Geology 48, 851–856. https://doi.org/10.1130/G47358.1.

Butler, R.W.H., 1992. Structural evolution of the western Chartreuse fold and thrust system, NW French Subalpine chains. In: McClay, K.R. (Ed.), Thrust Tectonics. Springer, Netherlands, Dordrecht, pp. 287–298. https://doi.org/10.1007/978-94-011-3066-0_26.

Carminati, E., Aldega, L., Smeraglia, L., Scharf, A., Mattern, F., Albert, R., Gerdes, A., 2020. Tectonic evolution of the Northern Oman mountains, part of the Strait of Hormuz Syntaxis: new structural and paleothermal analyses and U-Pb dating of Synkinematic Calcite. Tectonics 39. https://doi.org/10.1029/2019TC005936 e2019TC005936.

Cenki-Tok, B., Darling, J.R., Rolland, Y., Dhuime, B., Storey, C.D., 2014. Direct dating of mid-crustal shear zones with synkinematic allanite: new in situ U-Th-Pb geochronological approaches applied to the Mont Blanc massif. Terra Nova 26, 29–37. https://doi.org/10.1111/ter.12066.

Chew, D.M., Petrus, J.A., Kamber, B.S., 2014. U-Pb LA–ICPMS dating using accessory mineral standards with variable common Pb. Chem. Geol. 363, 185–199. https://doi.org/10.1016/j.chemgeo.2013.11.006.

Collombet, M., Thomas, J.C., Chauvin, A., Tricart, P., Bouillin, J.P., Gratier, J.P., 2002. Counterclockwise rotation of the western Alps since the Oligocene: new insights from paleomagnetic data. Tectonics 21, 14-1.

Corsini, M., Rolland, Y., 2009. Late evolution of the southern European Variscan belt: exhumation of the lower crust in a context of oblique convergence. Compt. Rendus Geosci. 341, 214–223.

Cruset, D., Vergés, J., Albert, R., Gerdes, A., Benedicto, A., Cantarero, I., Travé, A., 2020. Quantifying deformation processes in the SE Pyrenees using U-Pb dating of fracture-filling calcites. J. Geol. Soc. 177, 1186–1196. https://doi.org/10.1144/jgs2020-014.

Curzi, M., Bernasconi, S.M., Billi, A., Boschi, C., Aldega, L., Franchini, S., Albert, R., Gerdes, A., Barberio, M.D., Looser, N., Carminati, E., 2021. U-Pb age of the 2016 Amatrice earthquake causative fault (Mt. Gorzano, Italy) and paleo-fluid circulation during seismic cycles inferred from inter- and co-seismic calcite. Tectonophysics 819, 229076. https://doi.org/10.1016/j.tecto.2021.229076.

Dennis, K.J., Affek, H.P., Passey, B.H., Schrag, D.P., Eiler, J.M., 2011. Defining an absolute reference frame for 'clumped' isotope studies of CO2. Geochim. Cosmochim. Acta 75, 7117–7131. https://doi.org/10.1016/j.gca.2011.09.025.

Deville, E., 2021. Structure of the tectonic frontof the Western Alps: control of fluid pressure and Halite occurrence on the Decollement processes. Tectonics 40. https://doi.org/10.1029/2020TC006591.

Drost, K., Chew, D., Petrus, J.A., Scholze, F., Woodhead, J.D., Schneider, J.W., Harper, D.A.T., 2018. An image mapping approach to U-Pb LA-ICP-MS carbonate dating and applications to direct dating of carbonate sedimentation. Geochem. Geophys. Geosyst. 19, 4631–4648. https://doi.org/10.1029/2018GC007850.

Eiler, J.M., 2007. "Clumped-isotope" geochemistry—the study of naturally-occurring, multiply-substituted isotopologues. Earth Planet. Sci. Lett. 262, 309–327. https://doi.org/10.1016/j.epsl.2007.08.020.

Gabitov, R., Migdisov, A., Nguyen, A., Van Hartesveldt, N., Perez-Huerta, A., Sadekov, A., Sauer, K.B., Baker, J., Paul, V., Caporuscio, F., 2021. Uptake of uranium by carbonate crystallization from reduced and oxidized hydrothermal fluids. Chem. Geol. 564, 120054.

Gabitov, R.I., Sadekov, A., Leinweber, A., 2014. Crystal growth rate effect on Mg/Ca and Sr/Ca partitioning between calcite and fluid: an in situ approach. Chem. Geol. 367, 70–82. https://doi.org/10.1016/j.chemgeo.2013.12.019.

Ganade, C.E., Cioffi, C.R., Machado, J.P., Miranda, T., Lopes, L.B., Weinberg, R.F., Celestino, M.A., Carvalho, B., Guillong, M., Roberts, N.M., 2022. Recurrent tectonic activity in northeastern Brazil during Pangea breakup: constraints from U-Pb carbonate dating. Geology 50 (8), 969–974. https://doi.org/10.1130/G50032.1.

Ghosh, P., Adkins, J., Affek, H., Balta, B., Guo, W., Schauble, E.A., Schrag, D., Eiler, J.M., 2006. 13C–18O bonds in carbonate minerals: A new kind of paleothermometer 18.

Gidon, M., 1990. Les décrochements et leur place dans la structuration du massif de la Chartreuse (Alpes occidentales françaises). Géologie alpine 66, 39–55.

Gidon, M., 1981. La structure de l'extrémité méridionale du massif de la Chartreuse aux abords de Grenoble et son prolongement en Vercors. Géologie alpine 57, 93–107.

Girault, J.B., Bellahsen, N., Bernet, M., Pik, R., Loget, N., Lasseur, E., Rosenberg, C.L., Balvay, M., Sonnet, M., 2022. Exhumation of the Western Alpine collisional wedge: new thermochronological data. Tectonophysics 822, 229155. https://doi.org/10.1016/j.tecto.2021.229155.

Goodfellow, B.W., Viola, G., Bingen, B., Nuriel, P., Kylander-Clark, A.R.C., 2017. Palaeocene faulting in SE Sweden from U-Pb dating of slickenfibre calcite. Terra Nova 29, 321–328. https://doi.org/10.1111/ter.12280.

Hansman, R.J., Albert, R., Gerdes, A., Ring, U., 2018. Absolute ages of multiple generations of brittle structures by U-Pb dating of calcite. Geology 46, 207–210. https://doi.org/10.1130/G39822.1.

Henkes, G.A., Passey, B.H., Grossman, E.L., Shenton, B.J., Pérez-Huerta, A., Yancey, T.E., 2014. Temperature limits for preservation of primary calcite clumped isotope paleotemperatures. Geochim. Cosmochim. Acta 139, 362–382.

Hoareau, G., Crognier, N., Lacroix, B., Aubourg, C., Roberts, N.M.W., Niemi, N., Branellec, M., Beaudoin, N., Suárez Ruiz, I., 2021. Combination of Δ47 and U-Pb dating in tectonic calcite veins unravel the last pulses related to the Pyrenean Shortening (Spain). Earth Planet. Sci. Lett. 553, 116636 https://doi.org/10.1016/j.epsl.2020.116636.

Hoefs, J., 2021. Variations of Stable Isotope Ratios in Nature. In: Hoefs, J. (Ed.), Stable Isotope Geochemistry, Springer Textbooks in Earth Sciences, Geography and Environment. Springer International Publishing, Cham, pp. 267–498. https://doi.org/10.1007/978-3-030-77692-3_3.

Huntington, K.W., Eiler, J.M., Affek, H.P., Guo, W., Bonifacie, M., Yeung, L.Y., Thiagarajan, N., Passey, B., Tripati, A., Daëron, M., Came, R., 2009. Methods and limitations of 'clumped' CO 2 isotope (Δ 47) analysis by gas-source isotope ratio mass spectrometry. J. Mass Spectrom. 44, 1318–1329. https://doi.org/10.1002/jms.1614.

Kalifi, A., Leloup, P.H., Sorrel, P., Galy, A., Demory, F., Spina, V., Huet, B., Quillévéré, F., Ricciardi, F., Michoux, D., 2021. Chronology of thrust propagation from an updated tectono-sedimentary framework of the Miocene molasse (western Alps). Solid Earth 12, 2735–2771.

Kelly, S.D., Newville, M.G., Cheng, L., Kemner, K.M., Sutton, S.R., Fenter, P., Sturchio, N.C., Spötl, C., 2003. Uranyl incorporation in natural calcite. Environ. Sci. Technol. 37, 1284–1287. https://doi.org/10.1021/es025962f.

Kim, S.-T., O'Neil, J.R., 1997. Equilibrium and nonequilibrium oxygen isotope effects in synthetic carbonates. Geochim. Cosmochim. Acta 61, 3461–3475. https://doi.org/10.1016/S0016-7037(97)00169-5.

Lamy-Chappuis, B., Angus, D., Fisher, Q.J., Yardley, B.W., 2016. The effect of CO2-enriched brine injection on the mechanical properties of calcite-bearing sandstone. Int. J. Greenhouse Gas Control 52, 84–95.

Lanzirotti, A., Hanson, G.N., 1995. U-Pb dating of major and accessory minerals formed during metamorphism and deformation of metapelites. Geochim. Cosmochim. Acta 59, 2513–2526. https://doi.org/10.1016/0016-7037(95)00146-8.

Lemoine, M., Bas, T., Arnaud-Vanneau, A., Arnaud, H., Dumont, T., Gidon, M., Bourbon, M., de Graciansky, P.-C., Rudkiewicz, J.-L., Megard-Galli, J., 1986. The continental margin of the Mesozoic Tethys in the Western Alps. Mar. Pet. Geol. 3, 179–199.

Li, Q., Parrish, R.R., Horstwood, M.S.A., McArthur, J.M., 2014. U-Pb dating of cements in Mesozoic ammonites. Chem. Geol. 376, 76–83. https://doi.org/10.1016/j.chemgeo.2014.03.020.

Lloyd, M.K., Ryb, U., Eiler, J.M., 2018. Experimental calibration of clumped isotope reordering in dolomite. Geochim. Cosmochim. Acta 242, 1–20.

Looser, N., Madritsch, H., Guillong, M., Laurent, O., Wohlwend, S., Bernasconi, S., 2021. Absolute age and temperature constraints on deformation along the Basal Décollement of the Jura Fold-and-Thrust Belt from carbonate U-Pb. Tectonics 40 e2020TC006439.

Mangenot, X., Deçoninck, J.-F., Bonifacie, M., Rouchon, V., Collin, P.-Y., Quesne, D., Gasparrini, M., Sizun, J.-P., 2019. Thermal and exhumation histories of the northern subalpine chains (Bauges and Bornes-France): evidence from forward thermal modeling coupling clay mineral diagenesis, organic maturity and carbonate clumped isotope (Δ 47) data: XXXX. Basin Res. 31, 361–379. https://doi.org/10.1111/bre.12324.

Marrett, R., Allmendinger, R.W., 1990. Kinematic analysis of fault-slip data. J. Struct. Geol. 12, 973–986. https://doi.org/10.1016/0191-8141(90)90093-E.

Moss, S., 1992. Organic maturation in the French Subalpine chains: regional differences in burial history and the size of tectonic loads. J. Geol. Soc. 149, 503–515. https://doi.org/10.1144/gsjgs.149.4.0503.

Mugnier, J.-L., Arpin, R., Thouvenot, F., 1987. Coupes équilibrées à travers le massif subalpin de la Chartreuse. Geodin. Acta 1, 125–137. https://doi.org/10.1080/09853111.1987.11105131.

Muirhead, D.K., Bond, C.E., Watkins, H., Butler, R.W.H., Schito, A., Crawford, Z., Marpino, A., 2020. Raman spectroscopy: an effective thermal marker in low temperature carbonaceous fold–thrust belts. Geol. Soc. Lond., Spec. Publ. 490, 135–151. https://doi.org/10.1144/SP490-2019-27.

Nielsen, S.B., Clausen, O.R., McGregor, E., 2017. basin%R o : a vitrinite reflectance model derived from basin and laboratory data. Basin Res. 29, 515–536. https://doi.org/10.1111/bre.12160.

Nollet, S., Koerner, T., Kramm, U., Hilgers, C., 2009. Precipitation of fracture fillings and cements in the Buntsandstein (NW Germany) 13.

Nouibat, A., Stehly, L., Paul, A., Schwartz, S., Bodin, T., Dumont, T., Rolland, Y., Brossier, R., Cifalps Team and AlpArray Working Group, A., 2022. Lithospheric transdimensional ambient-noise tomography of W-Europe: implications for crustal-scale geometry of the W-Alps. Geophys. J. Int. 229, 862–879. https://doi.org/10.1093/gji/ggab520.

Ortega, R., Maire, R., Devès, G., Quinif, Y., 2005. High-resolution mapping of uranium and other trace elements in recrystallized aragonite–calcite speleothems from caves in the Pyrenees (France): implication for U-series dating. Earth Planet. Sci. Lett. 237, 911–923. https://doi.org/10.1016/j.epsl.2005.06.045.

Ortner, H., Reiter, F., Acs, P., 2002. Easy handling of tectonic data: the programs TectonicVB for Mac and TectonicsFP for Windowst$ 8.

Pagel, M., Bonifacie, M., Schneider, D.A., Gautheron, C., Brigaud, B., Calmels, D., Cros, A., Saint-Bezar, B., Landrein, P., Sutcliffe, C., Davis, D., Chaduteau, O., 2018. Improving paleohydrological and diagenetic reconstructions in calcite veins and breccia of a sedimentary basin by combining Δ47 temperature, δ18Owater and U-Pb age. Chem. Geol. 481, 1–17. https://doi.org/10.1016/j.chemgeo.2017.12.026.

Parizot, O., Missenard, Y., Barbarand, J., Blaise, T., Benedicto, A., Haurine, F., Sarda, P., 2022. How sensitive are intraplate inherited structures? Insight from the Cévennes Fault System (Languedoc, SE France). Geol. Mag. 1–13.

Parizot, O., Missenard, Y., Haurine, F., Blaise, T., Barbarand, J., Benedicto, A., Sarda, P., 2021. When did the Pyrenean shortening end? Insight from U-Pb geochronology of syn-faulting calcite (Corbières area, France). Terra Nova 33, 551–559. https://doi.org/10.1111/ter.12547.

Parrish, R.R., Parrish, C.M., Lasalle, S., 2018. Vein calcite dating reveals Pyrenean orogen as cause of Paleogene deformation in southern England. J. Geol. Soc. 175, 425–442. https://doi.org/10.1144/jgs2017-107.

Pascal, C., 2021. Paleostress Inversion Techniques: Methods and Applications for Tectonics, 1st ed. Elsevier, Amsterdam, The Netherlands.

Passey, B.H., Levin, N.E., Cerling, T.E., Brown, F.H., Eiler, J.M., 2010. High-temperature environments of human evolution in East Africa based on bond ordering in paleosol carbonates. Proc. Nat. Acad. Sci. 107, 11245–11249. https://doi.org/10.1073/pnas.1001824107.

Paton, C., Hellstrom, J., Paul, B., Woodhead, J., Hergt, J., 2011. Iolite: Freeware for the visualisation and processing of mass spectrometric data. J. Anal. At. Spectrom. 26, 2508. https://doi.org/10.1039/c1ja10172b.

Peyrotty, G., Brigaud, B., Martini, R., 2020. δ18O, δ13C, trace elements and REE in situ measurements coupled with U-Pb ages to reconstruct the diagenesis of upper triassic atoll-type carbonates from the Panthalassa Ocean. Mar. Pet. Geol. 120, 104520 https://doi.org/10.1016/j.marpetgeo.2020.104520.

Philippe, Y., Deville, E., Mascle, A., 1998. Thin-skinned inversion tectonics at oblique basin margins: example of the western Vercors and Chartreuse Subalpine massifs (SE France). Geol. Soc. Lond., Spec. Publ. 134, 239–262. https://doi.org/10.1144/GSL.SP.1998.134.01.11.

Prajapati, N., Selzer, M., Nestler, B., Busch, B., Hilgers, C., 2018. Modeling fracture cementation processes in calcite limestone: a phase-field study. Geotherm Energy 6, 7. https://doi.org/10.1186/s40517-018-0093-4.

Rasbury, E.T., Cole, J.M., 2009. Directly dating geologic events: U-Pb dating of carbonates. Rev. Geophys. 47, RG3001. https://doi.org/10.1029/2007RG000246.

Rasbury, E.T., Hanson, G.N., Meyers, W.J., Holt, W.E., Goldstein, R.H., Saller, A.H., 1998. U-Pb dates of paleosols: constraints on late Paleozoic cycle durations and boundary ages. Geology 26, 403–406. https://doi.org/10.1130/0091-7613(1998)026<0403:UPDOPC>2.3.CO;2.

Rasbury, E.T., Hanson, G.N., Meyers, W.J., Saller, A.H., 1997. Dating of the time of sedimentation using U-Pb ages for paleosol calcite. Geochim. Cosmochim. Acta 61, 1525–1529. https://doi.org/10.1016/S0016-7037(97)00043-4.

Rasbury, E.T., Meyers, W.J., Hanson, G.N., Goldstein, R.H., Saller, A.H., 2000. Relationship of uranium to petrography of caliche paleosols with application to precisely dating the time of sedimentation. J. Sediment. Res. 70, 604–618. https://doi.org/10.1306/2DC4092B-0E47-11D7-8643000102C1865D.

Reeder, R.J., Nugent, M., Lamble, G.M., Tait, C.D., Morris, D.E., 2000. Uranyl incorporation into calcite and aragonite: XAFS and luminescence studies. Environ. Sci. Technol. 34, 638–644. https://doi.org/10.1021/es990981j.

Ring, U., Gerdes, A., 2016. Kinematics of the Alpenrhein-Bodensee graben system in the Central Alps: Oligocene/Miocene transtension due to formation of the Western Alps arc: Alpenrhein-Bodensee graben system. Tectonics 35, 1367–1391. https://doi.org/10.1002/2015TC004085.

Roberts, G.P., 1994. Displacement localization and palaeo-seismicity of the Rencurel Thrust Zone, French Sub-Alpine chains. J. Struct. Geol. 16, 633–646. https://doi.org/10.1016/0191-8141(94)90115-5.

Roberts, N.M., Holdsworth, R.E., 2022. Timescales of faulting through calcite geochronology: a review. J. Struct. Geol. 104578.

Roberts, N.M.W., Drost, K., Horstwood, M.S.A., Condon, D.J., Chew, D., Drake, H., Milodowski, A.E., McLean, N.M., Smye, A.J., Walker, R.J., Haslam, R., Hodson, K., Imber, J., Beaudoin, N., Lee, J.K., 2020. Laser ablation inductively coupled plasma mass spectrometry (LA-ICP-MS) U-Pb carbonate geochronology: strategies, progress, and limitations. Geochronology 2, 33–61. https://doi.org/10.5194/gchron-2-33-2020.

Roberts, N.M.W., Rasbury, E.T., Parrish, R.R., Smith, C.J., Horstwood, M.S.A., Condon, D.J., 2017. A calcite reference material for LA-ICP-MS U-Pb geochronology. Geochem. Geophys. Geosyst. 18, 2807–2814. https://doi.org/10.1002/2016GC006784.

Roberts, N.M.W., Walker, R.J., 2016. U-Pb geochronology of calcite-mineralized faults: absolute timing of rift-related fault events on the Northeast Atlantic margin. Geology 44, 531–534. https://doi.org/10.1130/G37868.1.

Roberts, N.M.W., Žák, J., Vacek, F., Sláma, J., 2021. No more blind dates with calcite: fluid-flow vs. Fault-slip along the Očkov thrust, Prague Basin. Geosci. Front. 12, 101143 https://doi.org/10.1016/j.gsf.2021.101143.

Rolland, Y., Bilau, A., Cardinal, T., Nouibat, A., Bienveignant, D., Boschetti, L., Schwartz, S., Bernet, M., 2022. Bridging the gap between long-term orogenic evolution (>10 Ma scale) and geomorphological processes that shape the Western Alps: insights from combined dating approaches. Geosciences 12, 393. https://doi.org/10.3390/geosciences12110393.

Rolland, Y., Lardeaux, J.-M., Jolivet, L., 2012. Deciphering orogenic evolution. J. Geodyn. 56, 1–6.

Rolland, Y., Rossi, M., 2016. Two-stage fluid flow and element transfers in shear zones during collision burial-exhumation cycle: insights from the Mont Blanc Crystalline Massif (Western Alps). J. Geodyn. 101, 88–108.

Rolland, Y., Rossi, M., Cox, S., Corsini, M., Mancktelow, N., Pennacchioni, G., Fornari, M., Boullier, A.-M., 2008. 40Ar/39Ar dating of synkinematic white mica: Insights from fluid-rock reaction in low-grade shear zones (Mont Blanc Massif) and constraints on timing of deformation in the NW external Alps. Geol. Soc. Lond., Spec. Publ. 299, 293–315. https://doi.org/10.1144/SP299.18.

Rollion-Bard, C., Mangin, D., Champenois, M., 2007. Development and application of oxygen and carbon isotopic measurements of biogenic carbonates by ion microprobe. Geostand. Geoanal. Res. 31, 39–50. https://doi.org/10.1111/j.1751-908X.2007.00834.x.

Rosenberg, C.L., Bellahsen, N., Rabaute, A., Girault, J.-B., 2021. Distribution, style, amount of collisional shortening, and their link to Barrovian metamorphism in the European Alps. Earth Sci. Rev. 222, 103774.

Schori, M., Zwaan, F., Schreurs, G., Mosar, J., 2021. Pre-existing basement faults controlling deformation in the Jura Mountains fold-and-thrust belt: insights from analogue models. Tectonophysics 814, 228980.

Schwartz, S., Gautheron, C., Audin, L., Dumont, T., Nomade, J., Barbarand, J., Pinna-Jamme, R., van der Beek, P., 2017. Foreland exhumation controlled by crustal thickening in the Western Alps. Geology 45, 139–142.

Simonetti, M., Carosi, R., Montomoli, C., Cottle, J.M., Law, R.D., 2020. Transpressive deformation in the southern european variscan belt: new insights from the aiguilles rouges massif (Western Alps). Tectonics 39 e2020TC006153.

Simon-Labric, T., Rolland, Y., Dumont, T., Heymes, T., Authemayou, C., Corsini, M., Fornari, M., 2009. 40 Ar/ 39 Ar dating of Penninic Front tectonic displacement (W Alps) during the lower Oligocene (31–34 Ma). Terra Nova 21, 127–136. https://doi.org/10.1111/j.1365-3121.2009.00865.x.

Smeraglia, L., Aldega, L., Billi, A., Carminati, E., Di Fiore, F., Gerdes, A., Albert, R., Rossetti, F., Vignaroli, G., 2019. Development of an intrawedge tectonic mélange by out-of-sequence thrusting, buttressing, and intraformational rheological contrast, Mt. Massico Ridge, Apennines,Italy. Tectonics 38, 1223–1249. https://doi.org/10.1029/2018TC005243.

Smeraglia, L., Fabbri, O., Choulet, F., Buatier, M., Boulvais, P., Bernasconi, S.M., Castorina, F., 2020. Syntectonic fluid flow and deformation mechanisms within the frontal thrust of a foreland fold-and-thrust belt: example from the Internal Jura, Eastern France. Tectonophysics 778, 228178. https://doi.org/10.1016/j.tecto.2019.228178.

Smeraglia, L., Looser, N., Fabbri, O., Choulet, F., Guillong, M., Bernasconi, S.M., 2021. U-Pb dating of middle Eocene-Pliocene multiple tectonic pulses in the Alpine foreland. Solid Earth 12, 2539–2551.

Smith, P.E., Farquhar, R.M., 1989. Direct dating of Phanerozoic sediments by the 238U–206Pb method. Nature 341, 518–521. https://doi.org/10.1038/341518a0.

Spang, J.H., 1972. Numerical method for dynamic analysis of Calcite Twin Lamellae. Geol. Soc. Am. Bull. 83, 467. https://doi.org/10.1130/0016-7606(1972)83[467:NMFDAO]2.0.CO;2.

Sternai, P., Sue, C., Husson, L., Serpelloni, E., Becker, T.W., Willett, S.D., Faccenna, C., Di Giulio, A., Spada, G., Jolivet, L., Valla, P., Petit, C., Nocquet, J.-M., Walpersdorf, A., Castelltort, S., 2019. Present-day uplift of the European Alps: evaluating mechanisms and models of their relative contributions. Earth Sci. Rev. 190, 589–604. https://doi.org/10.1016/j.earscirev.2019.01.005.

Stolper, D.A., Eiler, J.M., 2015. The kinetics of solid-state isotope-exchange reactions for clumped isotopes: a study of inorganic calcites and apatites from natural and experimental samples. Am. J. Sci. 315, 363–411. https://doi.org/10.2475/05.2015.01.

Swart, P.K., Burns, S.J., Leder, J.J., 1991. Fractionation of the stable isotopes of oxygen and carbon in carbon dioxide during the reaction of calcite with phosphoric acid as a function of temperature and technique. Chem. Geol. Isotope Geosci. Sect. 86, 89–96. https://doi.org/10.1016/0168-9622(91)90055-2.

Tartese, R., Boulvais, P., Poujol, M., Gloaguen, E., Cuney, M., 2013. Uranium mobilization from the Variscan Questembert Syntectonic Granite during. Econ. Geol. 108, 379–386. https://doi.org/10.2113/econgeo.108.2.379.

Turner, F.J., 1953. Nature and dynamic interpretation of deformation lamellae in calcite of three marbles. Am. J. Sci. 251, 276–298.

Uysal, I., Feng, Y., Zhao, J., Altunel, E., Weatherley, D., Karabacak, V., Cengiz, O., Golding, S., Lawrence, M., Collerson, K., 2007. U-series dating and geochemical tracing of late Quaternary travertine in co-seismic fissures. Earth Planet. Sci. Lett. 257, 450–462. https://doi.org/10.1016/j.epsl.2007.03.004.

Uysal, I.T., Feng, Y., Zhao, J., Bolhar, R., Işik, V., Baublys, K.A., Yago, A., Golding, S.D., 2011. Seismic cycles recorded in late Quaternary calcite veins: geochronological, geochemical and microstructural evidence. Earth Planet. Sci. Lett. 303, 84–96. https://doi.org/10.1016/j.epsl.2010.12.039.

Veizer, J., Ala, D., Azmy, K., Bruckschen, P., Buhl, D., Bruhn, F., Carden, G.A.F., Diener, A., Ebneth, S., Godderis, Y., Jasper, T., Korte, C., Pawellek, F., Podlaha, O.G., Strauss, H., 1999. 87Sr86Sr, d13C and d18O evolution of Phanerozoic seawater 30.

Vermeesch, P., 2018. IsoplotR: a free and open toolbox for geochronology. Geosci. Front. 9, 1479–1493. https://doi.org/10.1016/j.gsf.2018.04.001.

Walpersdorf, A., Pinget, L., Vernant, P., Sue, C., Deprez, A., the RENAG team, 2018. Does long-term GPS in the Western Alps finally confirm earthquake mechanisms? Tectonics 37, 3721–3737. https://doi.org/10.1029/2018TC005054.

Weremeichik, J.M., Gabitov, R.I., Thien, B.M.J., Sadekov, A., 2017. The effect of growth rate on uranium partitioning between individual calcite crystals and fluid. Chem. Geol. 450, 145–153. https://doi.org/10.1016/j.chemgeo.2016.12.026.

Williams, R.T., Mozley, P.S., Sharp, W.D., Goodwin, L.B., 2019. U-Th dating of syntectonic calcite veins reveals the dynamic nature of fracture cementation and healing in faults. Geophys. Res. Lett. 46, 12900–12908.

Woodhead, J.D., Hergt, J.M., 2001. Strontium, neodymium and lead isotope analyses of NIST glass certified reference materials: SRM 610, 612, 614. Geostand. Geoanal. Res. 25, 261–266. https://doi.org/10.1111/j.1751-908X.2001.tb00601.x.